Applied Energy 402 (2026) 126987

Contents lists available at ScienceDirect

Applied Energy

journal homepage: www.elsevier.com/locate/apen

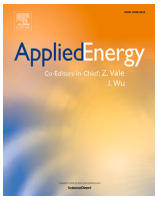

# Physics-informed operator learning for real-time battery state estimation

Lorenzo Brancato, Alexander Gabriel Harej, Marco Giglio, Francesco Cadini*

*Politecnico di Milano, Dipartimento di Meccanica, Via La Masa, 1, Milano, 20156, MI, Italy*

## HIGHLIGHTS

- Physics-informed neural operators enable real-time battery state estimation.
- MIONet surpasses OCFE and Padé methods in computational efficiency.
- Robust SOC prediction under dynamic EV and HEV operating conditions.
- Generalizable framework adaptable across battery chemistries and designs.
- Electrochemical model-based observer outperforms ECM in accuracy and precision.

## ARTICLE INFO

*Keywords:*
Battery management system
Operator learning
Physics-informed
Model order reduction
Online state estimation

## ABSTRACT

The rapid growth of electric vehicles (EVs) and hybrid electric vehicles (HEVs) has heightened the demand for efficient and safe lithium-ion (Li-ion) battery management systems (BMSs). Accurate state monitoring, such as state of charge (SOC) and state of health (SOH), is essential to prolong battery lifespan and ensure reliable EV performance. Although equivalent circuit models (ECMs) are widely used in BMSs for their simplicity, they provide limited insight into internal battery processes and struggle with high-dynamic applications. Physics-based models, particularly the Doyle-Fuller-Newman (DFN) model, offer a detailed representation of battery behavior, but their complexity demands model order reduction (MOR) for real-time applications. In recent years, deep learning, specifically operator learning techniques like the physics-informed multiple-input operator network (MIONet), has shown promising results in approximating complex partial differential equations (PDEs). In this work, we develop a physics-informed operator learning framework that learns the solution of Fick's law within the Single Particle Model (SPM). Our results demonstrate the superior computational efficiency and accuracy of this approach compared to established MOR methods. Furthermore, we demonstrate the flexibility of the method, which can be seamlessly retrained for different battery chemistries provided that the underlying physics remains unchanged. Finally, we evaluate the framework's effectiveness in SOC estimation tasks by embedding the reduced-order model within an observer, showing its potential to outperform traditional ECM-based methods. This study underscores the promise of operator learning in advancing BMSs development, paving the way for more reliable and efficient battery management in EVs and HEVs applications.

## 1. Introduction

In recent years, electric vehicles (EVs) and hybrid electric vehicles (HEVs) have experienced rapid growth due to a combination of environmental, economic, and technological factors [1]. As concerns about climate change and air pollution intensify, consumers and governments increasingly prioritize sustainable and environmentally friendly alternatives to traditional gasoline-powered vehicles [2]. This shift is driven by advances in EV/HEV technology that have significantly improved the performance, range, and affordability of these vehicles. A key component driving the efficiency and viability of electric vehicles is the lithium-ion (Li-ion) battery, which offers higher energy density, longer lifespan, faster charging times, and lower costs compared to other battery technologies [3–5].

Li-ion batteries are one of the most expensive components of an EV, making it essential to ensure their efficient use and to extend their lifespan by mitigating degradation and avoiding issues such as overheating and explosions. Achieving these objectives requires the development of an advanced battery management system (BMS) [6]

* Corresponding author.
*Email address:* francesco.cadini@polimi.it (F. Cadini).

https://doi.org/10.1016/j.apenergy.2025.126987
Received 19 May 2025; Received in revised form 9 October 2025; Accepted 26 October 2025
Available online 6 November 2025

**Nomenclature**

*Abbreviations*

BMS Battery Management System
CWC Coverage Width-Based Criterion
DeepONet Deep Operator Network
DFN Doyle-Fuller-Newman
ECM Equivalent Circuit Model
EKF Extended Kalman Filter
EV Electric Vehicle
FDM Finite-Difference Method
FVM Finite Volume Method
GRF Gaussian Random Field
HEV Hybrid Electric Vehicle
HPPC Hybrid Pulse Power Characterization
KF Kalman Filter
LFP Lithium Iron Phosphate
Li-ion Lithium-Ion
MCU Micro Controller Unit
MIONet Multiple-Input Operator Network
MOR Model Order Reduction
MPIW Mean Prediction Interval Width
MSE Mean Squared Error
NMC Nickel Manganese Cobalt
NN Neural Network
OCFE Orthogonal Collocation on Finite Elements
OCP Open-Circuit Potential
OCV Open-Circuit Voltage
ODE Ordinary Differential Equation
PDE Partial Differential Equation
PF Particle Filter
PICP Prediction Interval Coverage Probability
PINN Physics-Informed Neural Network
RC Resistance-Capacitance
RMSE Root Mean Squared Error
ROM Reduced-Order Model
SOC State of Charge
SOH State of Health
SPM Single Particle Model
SPMe Single Particle Model with electrolyte
UDDS Urban Dynamometer Driving Schedule
UKF Unscented Kalman Filter
UT Unscented Transform

capable of monitoring critical internal states, such as the state of charge (SOC) and the state of health (SOH), to ensure safe and efficient operation throughout the battery's lifecycle. Since these internal states are not directly observable with prevailing sensor technologies, they must be estimated from measurable quantities like current and voltage, which are crucial for BMSs functionality. Consequently, a suitable mathematical representation of the battery cell is often necessary in the design of model-based methods for state/parameter estimators and control strategies [7,8]. The accuracy achievable with these methods depends on the chosen battery cell model.

Phenomenological equivalent circuit models (ECMs) are widely used in BMSs development due to their simplicity, ease of implementation, and low computational demands [8–10]. ECMs emulate battery dynamics using an electrical circuit composed of elements like capacitors, resistors, inductors, and controlled voltage/current sources. A typical ECM with $n$ parallel RC branches represents each parameter (e.g., resistances R and capacitances C) as a function of the battery's SOC and temperature. Identifying these functions requires extensive offline testing and real-time parameter tracking [11]. Consequently, low-order ECMs are well-suited for applications with moderate operational demands, such as portable electronics, overnight EV charging, and renewable energy smoothing, where the model's limitations are manageable. However, ECMs face challenges in high-dynamic, high-power applications, such as those typically encountered in EVs and HEVs. Achieving sufficient model accuracy in such conditions requires increasing the model order, function complexity, and testing efforts [11]. Moreover, because the components of ECMs do not directly correspond to the electrochemical processes of the battery, ECMs provide limited insight into meaningful physical parameters, degradation mechanisms, or internal safety constraints, which can lead to inaccurate predictions of battery performance as batteries degrade over time [12]. This lack of predictive insight complicates efforts to maximize battery performance, a key concern in applications with stringent safety and performance standards. To mitigate these limitations, commercial Li-ion battery systems are often designed conservatively, which leads to increased size, weight, and cost.

To fully harness the potential of Li-ion batteries, physics-based models grounded in electrochemical principles are advantageous for developing the future generation of BMSs [6]. The widely adopted Doyle-Fuller-Newman (DFN) model exemplifies one such approach [13–15]. It uses partial differential equations (PDEs) and algebraic equations to describe spatial and temporal behaviors, such as Li-ion concentration and potential in both the electrode solid phase and electrolyte. The adaptability of the DFN model enables the modeling of batteries with different chemistries [16–19] and the inclusion of side reactions to simulate aging effects, such as growth of the solid electrolyte interphase film and lithium plating [20]. This makes the DFN model valuable for BMS applications aimed at extending battery life by capturing localized aging phenomena, which are challenging to address with conventional ECMs.

For practical BMS functions like state estimation, fault diagnosis, and power prediction, model order reduction (MOR) techniques are essential to reduce the computational complexity of the DFN model. MOR allows complex models to be simplified for real-time application without sacrificing key dynamics. Advances in microprocessor technology have enabled the implementation of high-fidelity reduced-order models (ROMs) of Li-ion batteries with a system order greater than 100 [19]. Nevertheless, low-order systems closer in complexity to ECMs are often preferable [21], particularly in designing BMS functionalities like online state estimation [22], parameter estimation [23], and fault diagnosis [24].

Numerous MOR techniques are used to simplify physics-based Li-ion battery models, generally categorized into four main approaches: spatial discretization, function approximation, frequency domain approximation, and simplified physics or spatial lumping [25]. In practical ROMs, assumptions are often made to exclude certain macroscale dynamics, simplifying complex couplings across submodels. The Single Particle Model (SPM) is one of the most simplified available ROM, providing adequate accuracy for low to moderate current applications with modest computational demand [26,27]. The Single Particle Model with electrolyte (SPMe) extends this framework by incorporating intra-cell concentration and potential variations, making it suitable for high-current applications while maintaining lower complexity compared to the DFN model [27]. Combining these models with MOR methods, such as function and frequency domain approximations, can further enhance their computational efficiency. Efficient ROMs frequently blend multiple MOR techniques to strike an optimal balance between accuracy and computational cost, a necessity for the practical deployment of physics-based models in advanced BMS applications.

Spatial discretization methods, such as the finite-difference method (FDM) and the finite-volume method (FVM), offer a straightforward

approach to ROM, where accuracy is enhanced by increasing the number of discretization nodes or control volumes at the expense of higher computational costs [28–31]. Function approximation methods, such as spectral methods, can achieve comparable accuracy with fewer nodes, making them more efficient for smooth spatial solutions [32]. Frequency domain approximation methods, such as residual grouping or Padé approximation, are effective for applications where batteries cycle within a narrow SOC range, as in HEVs or grid frequency regulation. However, these methods are limited when addressing large signal variations due to their reliance on linear assumptions [33]. Even the most streamlined physics-based ROMs still incur non-trivial online computation for real-time implementation. This has motivated parallel efforts to bypass detailed electrochemical models entirely and instead learn the state-of-charge mapping directly from data.

Recent advances in computational power and artificial intelligence have enabled data-driven methods for SOC/SOH estimation. These approaches typically use artificial neural networks (NNs) to model the battery as a black box, without requiring any information about its internal electrochemical structure [6,34]. NN-based SOC/SOH estimators commonly take terminal voltage, current, and ambient temperature as inputs and return the SOC/SOH as output. This approach avoids the need for internal parameter identification and physical modeling. Examples of NN-based SOC/SOH estimators can be found in [35–40]. The primary advantage of these black-box models is their simplicity, computational efficiency, and flexibility. Once trained, NN models are extremely fast to evaluate, making them highly suitable for real-time implementation in BMSs. However, they depend heavily on large quantities of training data, which can be difficult and time-consuming to collect in real-world experiments. Furthermore, because they do not incorporate any physical constraints, purely data-driven NNs may lack robustness under non-nominal or previously unseen operating conditions.

Bridging the gap between purely physics-based and purely data-driven approaches, recent work has explored the use of deep learning techniques for solving PDEs, such as those associated with the DFN model and its simplified variants (i.e., the SPM and SPMe). The universal approximation theorem provides the theoretical foundation for deep learning, asserting that NNs can approximate any continuous function [41]. Additionally, an extension of this theorem states that a NN can approximate any continuous non-linear functional or operator, defined as a mapping between functions [42,43]. Leveraging this foundation, Lu et al. [44] introduced the deep operator network (DeepONet), designed to facilitate the learning of explicit and implicit operators, as exemplified by PDEs. This architecture has also been adapted to a physics-informed framework [45] to address the data scarcity inherent in real-world applications, where data acquisition is often costly and sparse. Jin et al. [46] further expanded upon this approach with the multiple-input operator network (MIONet), a more general architecture that can handle multiple input functions, enabling the learning of more complex operators. Thus, operator learning shows potential as a novel MOR framework for constructing ROMs.

In the field of battery research, in recent years diverse studies have focused on the application of physics-based machine learning to enhance state estimation [47–52]. Concerning model-based algorithms, Zheng et al. pioneered a physics-informed MIONet to approximate the state-space representation of the PDE governing the evolution of solid-particle concentration in an extended SPM [53]. In their work, the authors used input concentration profiles and currents sampled from offline constant-discharge simulations performed at different C-rates with a numerical solver to generate the training database. Consequently, they validated their approach solely against constant positive-current profiles at different C-rates. However, investigating the performance of this approach under more challenging input-current profiles, such as those representative of dynamic EV/HEV operation (e.g., the UDDS profile), is crucial. Accounting for these highly dynamic inputs may also require redesigning the training process to enable the operator network to accurately map such complex inputs. Furthermore, no comparison has been made with other established MOR methods to assess the method's relative efficiency, nor with classical ECM-based methods when the surrogate model is embedded in an observer for online estimation of critical states (e.g., SOC) to assess the potential superiority in accuracy and precision of ECM-based observers.

Differently from Zheng et al. [53], who validated a physics-informed MIONet surrogate only under constant-current discharges, the present work improves and generalizes the physics-informed MIONet training strategy, and extends the investigation to highly dynamic load profiles. Furthermore, in this work we explicitly integrate the surrogate model into a state observer for online SOC estimation, and offer a direct comparison with existing MOR and ECM-based approaches. The key novelties and contributions can be summarised as follows:

- Development of a physics-informed MIONet surrogate for the efficient state-space representation of the SPM, enabling direct integration into a model-based observer.
- A purely physics-informed training strategy that, unlike Zheng et al. [53], avoids pre-computed labeled datasets and numerical PDE solutions. Initial conditions and current inputs are sampled from Gaussian random fields and Gaussian distributions, following the methodology of physics-informed DeepONet pioneers [54]. This approach eliminates the need to synthetically generate initial-condition datasets, reduces the computational cost of offline simulations, and enhances model prediction under unseen initial conditions and inputs.
- Comprehensive validation under non-constant current profiles, including both charging and discharging phases, as well as varying environmental temperatures, and demonstration of the framework's adaptability to different chemistries with minimal retraining using transfer learning.
- A comparative analysis with established MOR techniques and an ECM-based observer to contextualize the proposed MOR method within BMS frameworks, proving its superior efficiency, accuracy and precision.

The work is organized as follows. Section 2 outlines the electrochemical model used to simulate Li-ion battery dynamics and presents our operator-network approach for reduced-order state-space formulation modeling. Section 3 details the training pipeline, demonstrates minimal retraining requirements for different chemistries governed by the same underlying PDEs, and compares (i) our method with two established first-principles MOR techniques and (ii) SOC estimation performance when paired with an observer against a standard equivalent-circuit model under realistic EV/HEV load profiles and varying ambient temperatures. Section 4 concludes with future research directions.

## 2. Methodology

### 2.1. Mathematical modeling of the battery cell

A Li-ion cell consists of a negative electrode, separator, and positive electrode between two current collectors (Fig. 1). Active material particles in each electrode store lithium, while the electrolyte enables ion transport during charge/discharge. We model the cell using the DFN framework [13–15], following the formulation in Ref. [27]. This model resolves lithium transport in solid particles and electrolyte, charge conservation in both phases, and electrode kinetics. Let $x^* \in [0, L^*]$ denote the through-thickness coordinate, and $r^* \in [0, R_k^*]$ the radial coordinate within spherical active particles of electrode $k \in \{n, p\}$. Domains are

$$\Omega_n^* = [0, L_n^*], \quad \Omega_s^* = [L_n^*, L^* - L_p^*], \quad \Omega_p^* = [L^* - L_p^*, L^*],$$

and variables carry subscripts for region $k \in \{n, s, p\}$ and phase (solid s, electrolyte e). The complete dimensional DFN equations and boundary conditions are listed in Table A.5, with parameters in Table A.6.

We nondimensionalise using the scaling in Eq. (A.2) (details in Appendix A.2), introducing time scales associated with the different

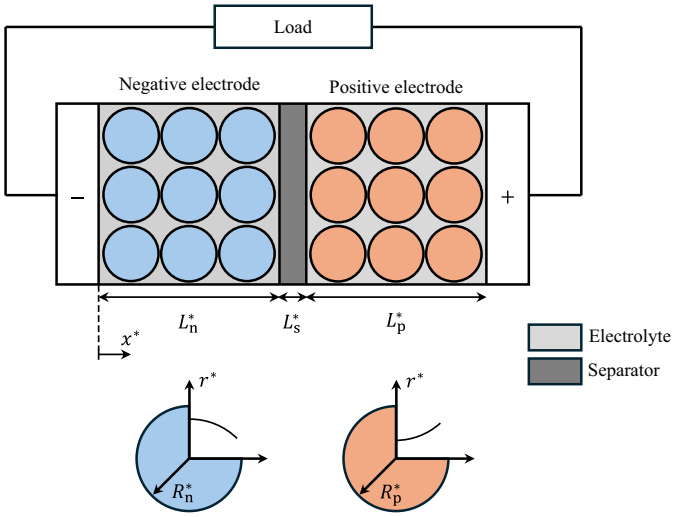


**Fig. 1.** Schematic of the DFN model for a battery cell, composed of anode, separator, cathode, and electrolyte.

physical processes and C-rate $C$. Dimensionless parameters are reported in Table A.7 and A.8. The resulting adimensional DFN equations are summarised in Table A.9.

The terminal voltage expression in the nondimensional DFN model can be written as

$$V = \bar{U}_p - \bar{U}_n + \eta_p - \eta_n + \text{Ohmic losses},$$

with the current path-wise decomposition and full derivation in Appendix A.2. Considering the high-conductivity, fast-electrolyte-transport limit (Appendix A.3) yields the Single Particle Model (SPM), reported in Table A.10. In the SPM, lithium diffusion is solved within one representative spherical particle per electrode, and potential drops in both phases are negligible at leading order. The leading-order cell voltage is

$$V^0 = \underbrace{\bar{U}_p(c^0_{s,p}|_{r=1}) - \bar{U}_n(c^0_{s,n}|_{r=1})}_{\text{OCV}} \underbrace{-2\sinh^{-1}\left(\frac{I}{j^0_{0,p} L_p}\right) - 2\sinh^{-1}\left(\frac{I}{j^0_{0,n} L_n}\right)}_{\text{Reaction overpotentials}}. \tag{1}$$

with $j^0_{0,k} = \frac{\gamma_k}{c_{r,k}}(c_{s,k})^{1/2}(1-c_{s,k})^{1/2}$. In the remainder, unless otherwise stated, the SPM is the electrochemical model embedded in the observer for SOC estimation, while the full DFN model, solved with PyBaMM [55], a Python-based framework for battery modeling, acts as the high-fidelity plant for generating synthetic validation data.

### 2.2. Physics-informed operator networks

The objective of this study is to leverage the operator learning capabilities of NNs to efficiently model the non-linear dynamics of the battery cell. It is well known that NNs are universal approximators of continuous functions $y \to f(y)$. By modifying the network structure and adapting the training process, it is also possible to approximate non-linear operators. Lu et al. proposed a specific NN structure called the DeepONet [44], which can learn various types of non-linear operators, including integrals, fractional Laplacians, and implicit operators that represent deterministic and stochastic differential equations. Let $G$ be an operator that takes an input function $u$, with $G(u)$ being the corresponding output function: $u(\cdot) \to G(u(\cdot))$. For any point $y$, called a coordinate, in the domain of $G(u)$, the output $G(u)(y)$ is a real number. Therefore, once trained, the DeepONet can predict the solution of the considered operator at any given coordinate $y$, when subjected to an arbitrary input

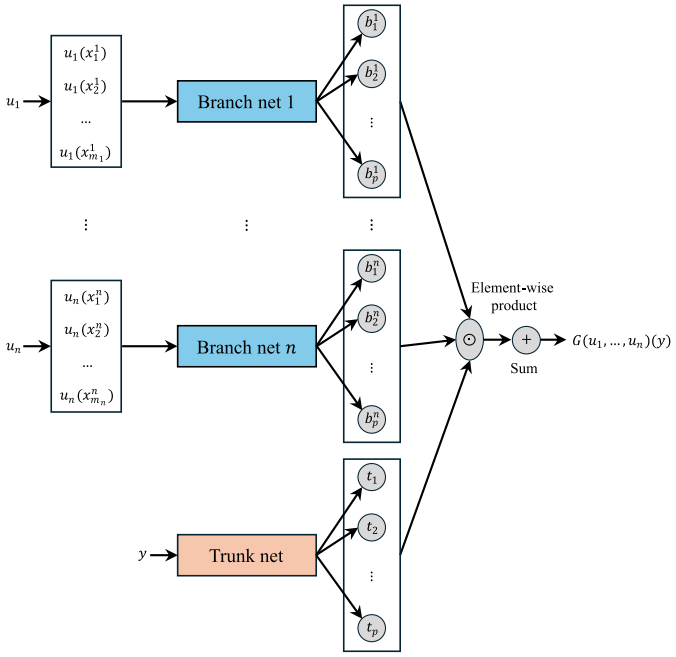


**Fig. 2.** The architecture of the MIONet. There are $n$ input functions $u_1,\ u_2,\ \ldots\ u_n$, each of them is discretized in a set of $m_i$ sensor points $\left\{x_1^i,\ x_2^i \ldots\ x_{m_i}^i\right\}$ and is fed into the respective branch network. The trunk network receives the coordinate vector $y$ as input. This vector contains the coordinates where the output function will be evaluated. The output layers of all branches must share the same length $p$, since they are merged through the scalar product.

function $u$. It is important to emphasize that operator networks, such as the DeepONet, are approximators of operators, thereby operating between sets of functions. In contrast, classical function approximators only approximate relationships between sets of scalars. However, the presented DeepONet structure has a significant limitation: it can only approximate operators from a single Banach space, where the input function is a single function. To overcome the limitation of handling a single input function from the DeepONet structure, Jin et al. [56] introduced the MIONet, which is capable of accepting more than one input function. Let $X_1, X_2, \ldots X_n$ and $Y$ be $n+1$ Banach spaces and $K_i \subset X_i\ (i = 1, 2 \ldots n)$ is a compact set, then the continuous operator $G$ can be defined as:

$$G:\ K_1 \times K_2 \times \ldots \times K_n \to Y, \qquad (u_1, u_2, \ldots, u_n) \to u$$

The MIONet architecture is similar to the DeepONet, and it is schematically illustrated in Fig. 2. The main difference is that the single branch network in DeepONet is replaced with multiple branch networks, each taking as input a different function $u_i(\cdot)$; indeed, there are as many branch networks as input functions. Each input function, $u_i(\cdot)$, fed into a branch net is discretized in a set of corresponding $m_i$ sensor points. The sensor points represent the number and the position of the coordinate points, where the input functions are discretized. It is not necessary that all branch networks share the same number of sensor points: different input functions can be discretized in different ways. The MIONet also consists of a single trunk network, which takes as input a vector containing the coordinates where the solution is evaluated. The output of the branch and the trunk network is then merged using a scalar product, which requires consistency in the dimensions of the output layers of all branch and trunk networks. The output of the MIONet, $\hat{G}$, can be computed according to Eq. (2):

$$\hat{G}\left(u_1, u_2, \ldots, u_n\right)(y) = \sum_{k=1}^{p}\left[\prod_{i=1}^{n} b_k^i\right] \cdot t_k \tag{2}$$

where $b_k^i$ is the $k$-th output node of the $i$-th branch net, and $t_k$ is the $k$-th output node of the trunk net.

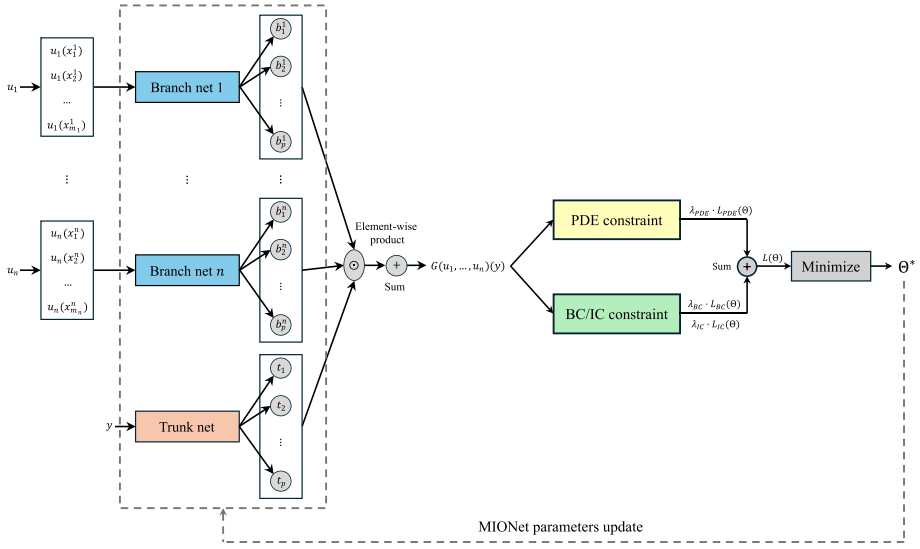


**Fig. 3.** Schematic representation of the physics-informed loss implementation and parameter update in MIONet. The learning process incorporates physics-based components into the loss function. Specifically, the total loss $L(\Theta)$ consists of the sum of three weighted terms: the PDE residual loss $L_{\text{PDE}}(\Theta)$, the boundary condition loss $L_{\text{BC}}(\Theta)$, and the initial condition loss $L_{\text{IC}}(\Theta)$, weighted by $\lambda_{\text{PDE}}, \lambda_{\text{BC}}$ and $\lambda_{\text{IC}}$, respectively. This total loss is used to update the MIONet parameters $\Theta$. A single training iteration involves computing $L(\Theta)$, followed by backpropagation to minimize the loss and obtain updated network weights $\Theta^*$. This framework enables the network to learn solutions that satisfy the underlying physical laws encoded in the PDE and boundary/initial conditions.

Unlike standard physics-informed neural networks (PINNs), which are designed to approximate particular solution fields, operator networks such as DeepONet and MIONet learn the mapping between entire function spaces. This property enables the operator network to generalize non-parametrically across initial conditions and input profiles, making it particularly well suited to surrogate the state-space formulation of electrochemical models, where the full state-transition dynamics must be represented rather than a single solution instance. In contrast, a PINN-based surrogate would typically require retraining for each new set of initial conditions or input profiles, making it impractical for online estimation in BMS applications.

To approximate the desired operator, the MIONet needs to be trained to learn the mapping between input and output function spaces. To avoid the computational complexity and time consumption associated with traditional discretization methods (e.g., finite difference or finite element methods) for generating training datasets, especially when dealing with complex operators, the MIONet can be trained using a purely physics-informed approach. This method leverages efficient automatic differentiation techniques to compute derivatives of the network's output with respect to its inputs. Consequently, the partial derivatives present in the PDEs describing a generic system can be obtained by differentiating the MIONet's output with respect to the trunk net inputs. These derivatives are then used to incorporate physical loss terms into the loss function during training.

In the case of a generic PDE system defined over a temporal-spatial domain with specified boundary and initial conditions, the total physical loss function can be split into three components: one loss enforcing the governing PDEs, one loss enforcing the boundary conditions (BC) and one loss enforcing the initial conditions (IC). Given the generic PDE system, $\mathcal{N}(u_1, u_2, \dots, u_n, G(u_1, u_2, \dots, u_n)) = 0$, subjected to generic boundary conditions, $\mathcal{B}(u_1, u_2, \dots, u_n, G(u_1, u_2, \dots, u_n)) = 0$, where $u_1, u_2, \dots, u_n$ are the input functions and $G(u_1, u_2, \dots, u_n)$ represents the solution of the operator to the corresponding input functions, the three loss terms are computed as shown below:

$$L_{\text{IC}} = \frac{\sum_{i=1}^{N_{\text{IC}}} \sum_{j=1}^{N_{y,\text{IC}}} \left[ G(u_1^{(i)}, u_2^{(i)}, \dots, u_n^{(i)})(y_j) - \hat{G}(u_1^{(i)}, u_2^{(i)}, \dots, u_n^{(i)})(y_j) \right]^2}{N_{\text{IC}} \times N_{y,\text{IC}}} \quad (3)$$

$$L_{\text{PDE}} = \frac{\sum_{i=1}^{N_{\text{PDE}}} \sum_{j=1}^{N_{y,\text{PDE}}} \left[ \mathcal{N}(u_1, u_2, \dots, u_n, \hat{G}(u_1, u_2, \dots, u_n)) \right]^2}{N_{\text{PDE}} \times N_{y,\text{PDE}}} \quad (4)$$

$$L_{\text{BC}} = \frac{\sum_{i=1}^{N_{\text{BC}}} \sum_{j=1}^{N_{y,\text{BC}}} \left[ \mathcal{B}(u_1, u_2, \dots, u_n, \hat{G}(u_1, u_2, \dots, u_n)) \right]^2}{N_{\text{BC}} \times N_{y,\text{BC}}} \quad (5)$$

where $\hat{G}(u_1, u_2, \dots, u_n)$ is the MIONet approximated solution of the operator $G$, $N_{\text{PDE}}$, $N_{\text{BC}}$, and $N_{\text{IC}}$ are the number of input functions sampled in each domain, and $N_{y,\text{PDE}}$, $N_{y,\text{BC}}$, and $N_{y,\text{IC}}$ are the number of collocation points within the respective domains. The total loss $L$ is the weighted sum of all the three physical terms:

$$L = \lambda_{\text{PDE}} \cdot L_{\text{PDE}} + \lambda_{\text{BC}} \cdot L_{\text{BC}} + \lambda_{\text{IC}} \cdot L_{\text{IC}} \quad (6)$$

The weights are used to balance the losses coming from different terms. A schematic representation of the MIONet trained utilizing a purely physics-informed loss, is illustrated in Fig. 3. In Section 3.1, we will demonstrate how the physics-informed MIONet can be trained and employed to define the state-space formulation of the SPM for a Li-ion battery cell.

### 2.3. Online state estimation

To estimate the internal states of a dynamical system, observers are commonly used to estimate the observable system states from the available measurements. The linear Kalman filter (KF) serves as the foundational framework for this purpose, providing optimal state estimates under the assumptions of linear dynamics and Gaussian noise [57]. However, real-world systems often exhibit non-linear behavior, rendering the linear KF inadequate. To address this limitation, the Extended Kalman Filter (EKF) was developed [58]. The EKF linearizes the system dynamics at each time step by propagating the state and covariance through the Jacobian of the non-linear state function. Although this approach extends the applicability of the KF to mildly non-linear systems, it introduces significant drawbacks: (i) linearization errors accumulate over time, particularly in highly non-linear regimes, and (ii) computing Jacobian matrices can be analytically complex or numerically unstable, especially for highly non-linear systems. These limitations degrade the accuracy and robustness of the EKF in practical scenarios. To circumvent

the reliance on linearization, the Unscented Kalman Filter (UKF) was proposed [59,60]. Instead of linearizing the system, the UKF employs a deterministic sampling technique known as the Unscented Transform (UT). This method strategically selects a minimal set of sigma points to approximate the system's probability distribution. These points are propagated directly through the non-linear state function, and the transformed distribution is reconstructed from their weighted statistics. By avoiding Jacobian computations and retaining the original non-linear dynamics, the UKF achieves higher fidelity in capturing the true statistical behavior of the system. This results in improved robustness and accuracy, especially in systems with strong non-linearities or discontinuous dynamics, where the EKF's linearization assumptions break down.

The UKF algorithm operates in two stages. First, during the prediction stage, $2N + 1$ sigma points ($\chi^i$) and their corresponding weights ($W^i$) are generated based on the previous state, $x[t]$, and covariance, $P_{xx}[t]$, estimate, according to Eq. (7):

$$\begin{aligned}
&\chi^0[t] = \bar{x}[t], \qquad W^0 = \kappa/(n+\kappa) \quad \kappa \in \Re \\
&\chi^i[t] = \bar{x}[t] + \left(\sqrt{(n+\kappa)\,P_{xx}[t]}\right)_i, \quad W^i = 1/2(n+\kappa) \quad i \in \{1,2\ldots N\} \\
&\chi^{i+N}[t] = \bar{x}[t] - \left(\sqrt{(n+\kappa)\,P_{xx}[t]}\right)_i, \quad W^{i+N} = 1/2(n+\kappa) \quad i \in \{1,2\ldots N\}
\end{aligned} \tag{7}$$

where $\left(\sqrt{(n+\kappa)\,P_{xx}[t]}\right)_i$ is the $i$-th row of the matrix $\sqrt{(n+\kappa)\,P_{xx}[t]}$, $n$ is the number of states, and $\kappa$ is an integer scaling factor that can reduce high order errors.

Note that there are different methods to determine the sigma points; in this work, we follow the method proposed by Julier et al. [61]. The computed sigma points are then propagated to the current time step, $t+1$, through the non-linear state-space function, denoted with $f$:

$$Y^i[t+1] = f\left(\chi^i[t]\right) \tag{8}$$

The propagated points are used to reconstruct the mean and the covariance of the state at the current step through the UT, using the weights previously defined in Eq. (7):

$$\bar{x}^-[t+1] = \sum_{i=0}^{2N} W^i Y^i[t+1] \tag{9a}$$

$$P_{xx}^-[t+1] = \sum_{i=0}^{2N} W^i (Y^i[t+1] - \bar{x}^-[t+1])\left(Y^i[t+1] - \bar{x}^-[t+1]\right)^T + Q \tag{9b}$$

where $Q$ is the covariance matrix of the process noise.

Second, the update stage follows the prediction stage: the propagated sigma points are mapped through the measurement function, $h$. Subsequently, the mean ($\mu_z$) and the covariance ($P_z$) of these points, along with the cross-covariance between the states and the measurement ($P_{xz}$), are estimated using the UT:

$$Z^i = h\left(Y^i\right) \tag{10a}$$

$$\mu_z = \sum_{i=0}^{2N} W^i Z^i \tag{10b}$$

$$P_{zz} = \sum_{i=0}^{2N} W^i (Z^i - \mu_z)\left(Z^i - \mu_z\right)^T + R \tag{10c}$$

$$P_{xz} = \sum_{i=0}^{2N} W^i (Y^i - \bar{x}_k(-))\left(Z^i - \mu_z\right)^T \tag{10d}$$

where $R$ is the covariance of the measurement noise.

Finally, the state and covariance predictions at the current time step are updated with the residual of the measurement, $z[t+1]$:

$$\bar{x}^+[t+1] = \bar{x}^-[t+1] + P_{xz} P_{zz}^{-1}\left(z[t+1] - \mu_z\right) \tag{11a}$$

$$P_{xx}^+[t+1] = P_{xx}^-[t+1] + \left(P_{xz} P_{zz}^{-1}\right) P_{zz}\left(P_{xz} P_{zz}^{-1}\right)^T \tag{11b}$$

In adapting the UKF to the electrochemical model, the hidden states represent the concentrations of lithium in the two electrodes, modeled as a single equivalent particle, while the measured quantity is the voltage. In contrast, the state function $f(\cdot)$ is derived from the PDEs of the SPM (Table A.10) using the physics-informed MIONet, while the measurement function $h(\cdot)$ is implemented in its analytical form, derived from Eq. (1). The scope of such defined observer, is to propagate the states from time instant $t$ to time instant $t+1$, using as input the current intensity, $I[t]$. Once the states are propagated to the next time step, the observer acts to update these values based on the measured terminal voltage $V[t]$. In practice, the observer recursively propagates and updates the state estimate based on the available measurements. In this way, it is possible to mitigate the errors coming from the measurements and from the model. Finally, from the estimated states, i.e., the concentration of lithium in the electrodes, it is possible to calculate the SOC of the Li-ion battery cell.

## 3. Results and discussion

In this section, we first address the training and the state-space formulation of the physics-informed MIONet, tailored to the problem of solving the SPM. The state-space formulation of the SPM is essential for embedding the considered EM into the UKF, which is necessary for performing online state estimation. We then present a comparison of the model surrogation performance between this method and two established MOR techniques. Once the state space model of the SPM is successfully formulated using the physics-informed MIONet and its computational efficiency is proven, it can be used for a practical implementation within the BMS. We demonstrate the advantage of replacing a physical electrochemical model, i.e., the SPM, with an observer, the UKF, when performing a critical BMS task, the online SOC estimation, under different realistic scenarios, representative of an EV/HEV operation.

### 3.1. MIONet training and state-space formulation

In this subsection, we address the development of the state-space model formulation for Li-ion concentration in electrode particles by training the MIONet in a purely physics-informed manner. The state-space model is essential for embedding the SPM into an observer for online state estimation. Referring to Table A.10, it is evident that the two concentrations of Li-ions in the electrodes serve as the system's states. As spatial functions, these concentrations are discretized along the radial coordinate into vectors $\boldsymbol{c}_{s,\mathrm{p}}$ and $\boldsymbol{c}_{s,\mathrm{n}}$, while the load current density, $I$, acts as the control input. The concentrations at the current time step, $t+1$, depend on the concentrations and the load current density value at the previous time step, $t$. The voltage, $V[t]$, at time step $t$ depends on the lithium concentrations in both electrodes and on current value. Since the two electrodes have different boundary conditions and parameters (see Table A.10 and A.8), the state-space formulation of the SPM can be written as:

$$\boldsymbol{c}_s[t+1] = \begin{pmatrix} \boldsymbol{c}_{s,\mathrm{p}}[t+1] \\ \boldsymbol{c}_{s,\mathrm{n}}[t+1] \end{pmatrix} = \begin{pmatrix} f_{\mathrm{p}}\left(\boldsymbol{c}_{s,\mathrm{p}}[t], I[t], \Delta t\right) \\ f_{\mathrm{n}}\left(\boldsymbol{c}_{s,\mathrm{n}}[t], I[t], \Delta t\right) \end{pmatrix} = f\left(\boldsymbol{c}_s[t], I[t]\right) \tag{12}$$

$$V[t] = h\left(\boldsymbol{c}_s[t], I[t]\right) \tag{13}$$

where $f$ is the state transition function and $h$ is the measurement function.

The objective now becomes designing and training the physics-informed MIONet to learn the two non-linear state functions $f_{\mathrm{p}}$ and $f_{\mathrm{n}}$, for the positive and negative electrodes, respectively. Therefore, two physics-informed MIONets are required, one for each electrode. Each physics-informed MIONet includes two branch networks because only two independent functions, the concentration profile and the current input at the previous time step, appear in the state functions of the

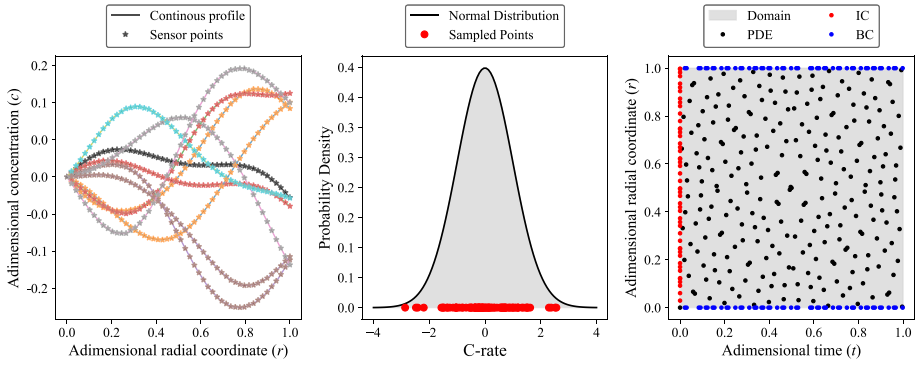


**Fig. 4.** (a) Example of initial concentration profiles sampled from a zero-mean GRF with squared exponential kernel and length scale factor, $\ell = 0.3$. (b) Example of input current scalar values sampled from a normal distribution with zero-mean and $\sigma = 1$ (95 % of points within $[-2, 2]$). (c) Example of $N_{y,\mathrm{IC}}$, $N_{y,\mathrm{BC}}$, and $N_{y,\mathrm{PDE}}$ collocation points; they are randomly sampled through Sobol sampling method.

two electrodes. The first branch network receives as input the lithium concentration, discretized into 50 equidistant sensor points ($m_1 = 50$). The second branch network takes as input the scalar value representing the intensity of the load current ($m_2 = 1$). The latter does not require discretization, as it is assumed to be constant within each time step (a negative value indicates charging, while a positive value indicates discharging of the battery). On the other side, the trunk network takes as input the coordinates at which the MIONet's output, i.e., the next state, is evaluated. For the SPM, these coordinates include the time and the radial coordinate, therefore, the trunk network has two input nodes. Each network consists of 7 hidden layers, following the aforementioned input layer, with 100 neurons per layer, all employing the hyperbolic tangent activation function. The layer parameters are initialized before training using Xavier normalization [62], and the biases are set to zero. The MIONet is trained using a purely physics-informed strategy. Referring to Fig. 3, the network is optimized by enforcing three distinct physical losses: PDE, BC, and IC. For each loss, $N_{\mathrm{PDE}}$, $N_{\mathrm{BC}}$, and $N_{\mathrm{IC}}$ input concentration profiles are generated from a Gaussian Random Field (GRF), following the physics-informed training approach in Ref. [45]. This procedure removes the need to solve the PDE system beforehand to build a database of plausible initial conditions, as in Ref. [53], and enhances the model's generalization capability to unseen inputs. A mean-zero GRF is defined as

$$c_{s,\mathrm{k}}(r) \sim \mathcal{GP}\left(0, k_\ell(r_1, r_2)\right),$$

where $r$ denotes a set of sensor points and the covariance kernel

$$k_\ell(r_1, r_2) = \exp\left(-\frac{\|r_1 - r_2\|^2}{2\ell^2}\right), \quad \ell = 0.3$$

is the squared exponential kernel. This generates random functions that broadly explore the space of possible initial concentration profiles. Likewise, $N_{\mathrm{PDE}}$, $N_{\mathrm{BC}}$, and $N_{\mathrm{IC}}$ current inputs are drawn from a zero-mean Gaussian distribution,

$$I \sim \mathcal{N}(0, 1),$$

ensuring adequate coverage of the scalar current space (with amplitude scaled in C-rate). Collocation points for evaluating each loss are chosen to efficiently cover the relevant domains. For the PDE loss, the spatio-temporal domain is uniformly mapped using the Sobol sequence [63], which provides good coverage with fewer points than purely random sampling. For the BC and IC losses, collocation points are randomly sampled within their respective temporal and spatial 1D domains. Fig. 4 illustrates this mapping of input functions and collocation points.

**Table 1**
Training hyperparameters.

| Loss term | No. of input functions ($N$) | No. of collocation points ($N_y$) | Loss weight ($\lambda$) |
|---|---|---|---|
| PDE | 150 | 10,000 | $10^{-2}$ |
| BC | 150 | 500 | 10 |
| IC | 1000 | 100 | $10^{3}$ |

Each physical loss term is computed over the following training datasets:

$$\text{PDE loss:} \quad \left(\left\{c_{s,\mathrm{k}}^{(i)}, I^{(i)}\right\}_{i=1}^{N_{\mathrm{PDE}}}, \left\{[t, r]^{(j)}\right\}_{j=1}^{N_{y,\mathrm{PDE}}}\right)$$

$$\text{BC loss:} \quad \left(\left\{c_{s,\mathrm{k}}^{(i)}, I^{(i)}\right\}_{i=1}^{N_{\mathrm{BC}}}, \left\{[t, r = 0/1]^{(j)}\right\}_{j=1}^{N_{y,\mathrm{BC}}}\right)$$

$$\text{IC loss:} \quad \left(\left\{c_{s,\mathrm{k}}^{(i)}, I^{(i)}\right\}_{i=1}^{N_{\mathrm{IC}}}, \left\{[t = 0, r]^{(j)}\right\}_{j=1}^{N_{y,\mathrm{IC}}}\right)$$

In total, there are $N_{\mathrm{PDE}} \times N_{y,\mathrm{PDE}}$ training samples for the PDE loss, $N_{\mathrm{BC}} \times N_{y,\mathrm{BC}}$ for the BC loss, and $N_{\mathrm{IC}} \times N_{y,\mathrm{IC}}$ for the IC loss. The dataset is split into 10 batches, and input functions are re-sampled every 100 epochs to improve coverage of the Banach space. Training hyperparameters for each loss are summarised in Table 1. The loss weights, $\lambda$, are used to balance the contributions coming from different terms. Their tuning is part of the training hyperparameters optimization. The authors recommend initially conducting shorter and simpler training runs, using fewer epochs and smaller datasets, to quickly assess whether the loss terms are properly balanced. A good balance is achieved when the numerical values of the distinct loss terms have a similar order of magnitude. If the losses are not well balanced, one term may dominate the training process, potentially hindering the learning of the others. An example of effective loss balancing is illustrated in Fig. 5(b), where all three loss terms remain within approximately the same magnitude and consistently decrease their amplitude throughout the training process.

During training, two different optimizers are sequentially employed following the approach suggested in Ref. [64], which ensures smoother and faster convergence of the physics-based loss functions, which are typically ill-conditioned. Initially, the Adam optimizer is set with a learning rate of $10^{-4}$. Once the training loss converges to a steady-state value, the optimizer switches to the L-BFGS optimizer, and training continues until convergence is achieved again. At each epoch, a validation loss is also computed using a labeled dataset. The reference solution is computed by solving the concentration field in the SPM using a finite-difference solver in Python implemented within the PyBaMM library

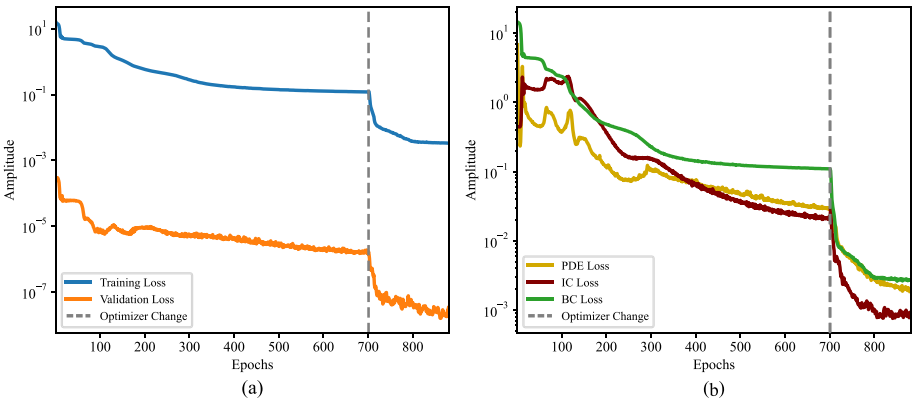


**Fig. 5.** (a) Example of training and validation loss for the negative-electrode MIONet. (b) Example of physical loss components for the negative-electrode MIONet.

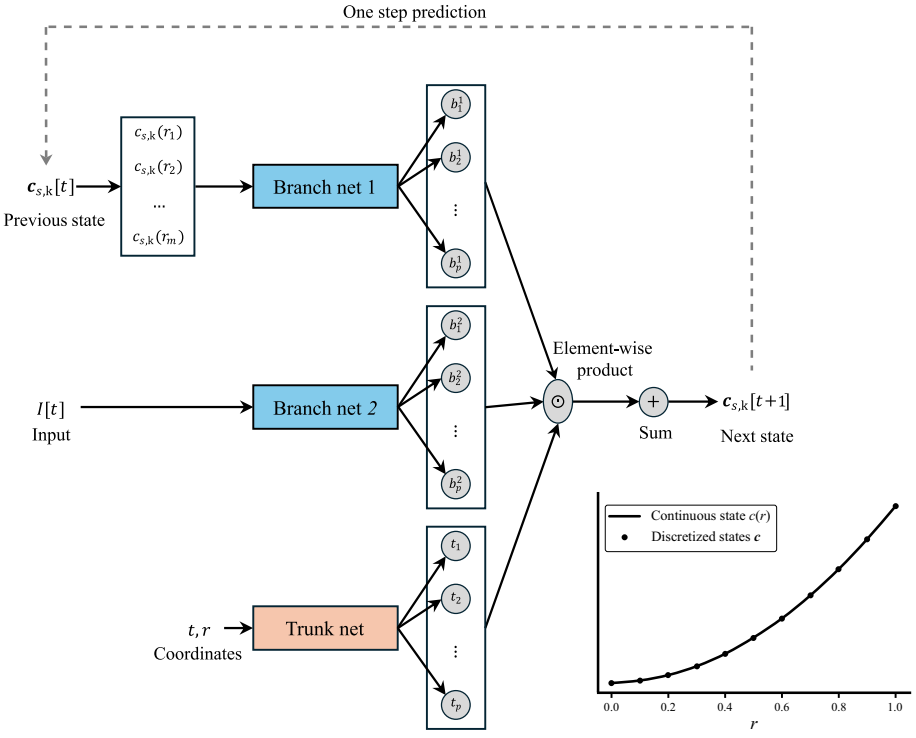


**Fig. 6.** Recursive state-space modeling with MIONet. The output concentration profile is used as the initial concentration profile for the next iteration. When the output concentration discretization does not correspond to the sensor discretization (i.e., when $\hat{N} \neq m$), interpolation is needed.

[55], and the validation loss is calculated as the Mean Squared Error (MSE) between the MIONet predictions and the reference solution. This validation loss offers a practical estimate of the model performance during training. For users who wish to completely avoid numerical solvers, it is still possible to validate the model using the physics-informed loss (Eqs. (3)–(6)), by specifying a validation set of input functions and collocation points. The evolutions of the training and validation loss functions are illustrated in Fig. 5, highlighting the point where the optimizer changes to demonstrate the variation in the learning slope. Training takes approximately 3 hours on an NVIDIA RTX A5000 GPU for each MIONet for both electrodes.

Once the MIONet training is completed, the state-space function can be formulated as previously shown in Eq. (12). The time step is set to 1 s ($\Delta t = 1\ s$), while the spatial discretization is not yet fixed, pending a performance analysis based on the optimal number of discretization points. However, the training process is designed to allow subsequent adjustment of the time step parameter. At each time step, the two MIONets (one for each electrode) receive as inputs the Li-ion concentrations from the previous time step and the current value. The MIONets output the Li-ion concentration at the next time step for the radial coordinates specified in the trunk network. If the chosen state vector size for the discretization of the concentration profiles does not coincide with the number of sensor points in the branch network, interpolation is needed before feeding it back into the branch network to evaluate the next step. The graphical representation of the state-space formulation of the MIONet is shown in Fig. 6.

### 3.2. MIONet generalization capability: transfer learning to a different battery chemistry

An important advantage of physics-informed approaches lies in their inherent generalization capability. When the governing physical laws remain the same, adapting a trained model to different cell chemistries and/or geometries can be achieved by simply updating the parameters

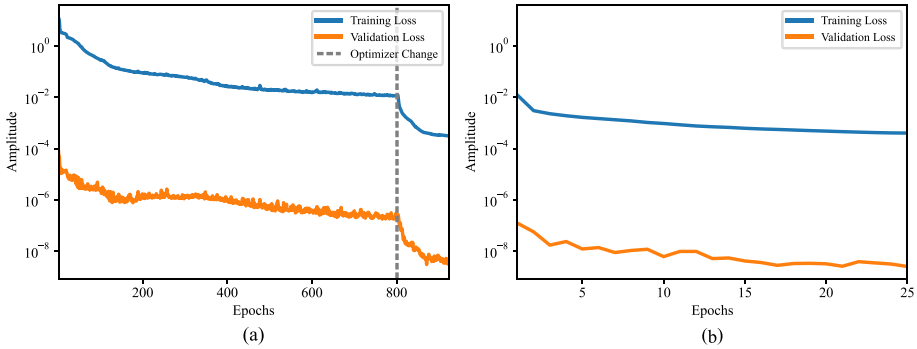


**Fig. 7.** (a) Training and validation loss for the positive-electrode MIONet trained from scratch on the LFP cell. (b) Training and validation loss for the positive-electrode MIONet adapted from the NMC cell to the LFP cell through transfer learning, showing rapid convergence to the same loss amplitude as the from-scratch-trained model.

of the underlying physical model. This allows the core learning architecture to retain its encoded physical knowledge, making "transfer" to new configurations both fast and efficient. To illustrate this, we adapted the MIONet originally trained on a Li-ion battery cell with a graphite negative electrode and a lithium nickel manganese cobalt oxide (NMC) positive electrode, whose parameters were taken from Ref. [65], to a lithium iron phosphate (LFP) cell with different electrode materials and dimensions, using parameters reported in Ref. [66]. We applied transfer learning by retaining the trained MIONet weights and retraining only with the L-BFGS optimizer for 25 epochs (which takes approximately only 15 min using the same GPU) with the learning rate set to 0.001, after updating the original parameters to match those of the LFP cell. For comparison, a model was also trained from scratch with the same LFP cell parameters. As shown in Fig. 7 the transfer learning approach rapidly reached the same physics-informed loss and validation loss magnitudes as the from-scratch-trained model, which required almost 1000 epochs (approximately 3 hours) to converge. The plot in Fig. 7 refers to the positive-electrode training. After training two MIONets, one for each electrode, we further assessed the accuracy of the retrained model in a 1 C-rate discharge scenario by performing recursive predictions of lithium concentration in both electrodes. The results showed estimation accuracy comparable to that of the original MIONets, confirming that transfer learning is an effective strategy to preserve the predictive capability across the full cell model. These results confirm that the proposed MIONet framework, grounded in physics-informed operator learning, is not only accurate for the target cell but also universal and stable across different chemistries and geometries, as long as the underlying physical laws are preserved. This effective transfer learning represents a major advantage of the proposed method, and of physics-based approaches in general, over purely empirical models such as ECMs, since changing the battery cell type, dimensions, or chemistry does not require performing new experimental campaigns to identify model parameters (e.g., resistances and capacitances in the ECM).

In the remainder of this section, unless otherwise stated, we will consider the MIONets trained on the NMC pouch cell.

### 3.3. Comparison with state-of-the-art MOR methods

This section demonstrates the computational advantages of the proposed approach by comparing its computational cost and accuracy of prediction against two established MOR methods, namely the OCFE and the Padé approximation. The necessity to compare the proposed and existing methods is twofold: first, to illustrate the viability of the proposed approach in terms of efficiency for solving complex battery electrochemical models; second, to demonstrate the efficacy of the proposed approach in facilitating the integration of the models within an observer for the tracking of critical battery internal states. The state function of the state-space model representation necessitates the implementation of an efficient and accurate discretization approach in real-time.

The OCFE is a discretization method that differs from the traditional finite element method, particularly in the way solutions are approximated and evaluated within each element. The traditional FE method utilizes local polynomial interpolation functions and integrates weighted residuals over each element, whereas OCFE discretizes the domain into finite elements and enforces the governing equations at specific collocation points. These points, typically chosen as roots of orthogonal polynomials, eliminate the need for numerical integration within elements, resulting in smaller, simpler, and more efficient algebraic systems. Consequently, OCFE generally achieves higher accuracy with fewer discretization points compared to the traditional FE method, provided that the solutions are sufficiently smooth functions. The number of states corresponds directly to the total number of discretization points in the spatial domain. In contrast, the Padé approximation is a method of approximating the transfer function of PDE-based systems using a ratio of two polynomials. The coefficients of these polynomials are determined by matching the Taylor series expansion of the function up to a specified order at a chosen expansion point. In contrast to OCFE or traditional FE methods, the Padé approximation does not solve the PDE across the entire spatial domain. Instead, it simplifies the solution by calculating only specific integral or boundary values. To illustrate this, consider the solution to the SPM. In this case, the Padé approximation calculates the average concentration along the radial coordinate and the surface concentration; it does not provide detailed spatial profiles within the domain. However, the actual number of states corresponds to the order of the polynomial used in the Padé approximation.

The comparison of the different MOR methods investigated is based on identifying the relationship between two key performance metrics: computational time per step and prediction accuracy. The simulation scenario under consideration has a duration of one hour, with a constant discharging rate of 1 C. The OCFE and the Padé approximation methods are implemented following the methodology outlined in Ref. [67,68], respectively. For all three methods, the state-space formulation is obtained, and the simulation is conducted through recursive propagation of states. The total number of states is the sum of the anode and cathode states. The computational time per step of each method is measured as the time required to propagate the states to the next time step, in milliseconds. Accuracy is quantified using the Frobenius norm of the difference between the predicted concentrations and the benchmark solution, which is obtained by solving the SPM equations in Python using the finite volume method implemented in the PyBaMM library. For clarity, the concentration of Li-ions in both electrodes is normalized to the interval $[0, 1]$. In the case of the Padé approximation, accuracy is assessed using the Frobenius norm of the average and surface concentration values over time, as the full spatial discretization is not available with this method. The prediction error and computational time per step are evaluated separately for each electrode and then averaged. The performance comparison is shown in Fig. 8. OCFE demonstrates the most significant

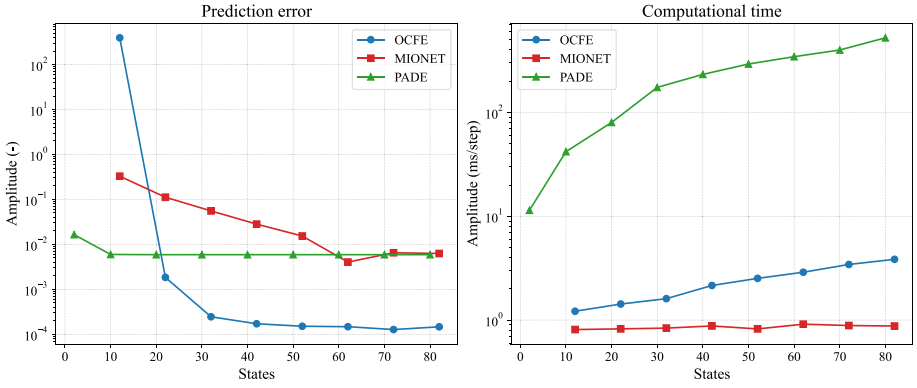


**Fig. 8.** (a) Comparison of prediction errors evolution with the number of discretization states. (b) Comparison of computational time increase with the number of discretization states.

improvement in accuracy as the number of states increases. At approximately 40 states (number of discretization points), the error stabilizes, and further increases in states do not yield substantial accuracy improvements. The Padé approximation attains its steady-state value with a relatively modest number of states (order of the transfer function approximation). This phenomenon can be attributed to the constant input current profile employed in the simulation, as just few orders are enough to approximate the dynamics for constant inputs. The MIONet stabilizes at approximately 60 states (number of sensor points), beyond which no further accuracy improvements occur. In terms of computational efficiency, the Padé approximation is the most time-consuming method, followed by OCFE. MIONet, conversely, is the most time-efficient discretization method. It is noteworthy that both Padé approximation and OCFE methods are significantly influenced by the number of states: as the number of states increases, computational time rises. In contrast, MIONet's computational time is almost unaffected by an increase in the number of states. It is important to note that time efficiency is a crucial parameter when embedding a state space model in the UKF, as the latter requires the propagation of additional states (the sigma points)), which further increase computational cost. Consequently, the time required for a single time step of the observer increases significantly, while the small error introduced by the discretization process in the observer is compensated for by the observer itself. In conclusion, the authors wish to emphasize the fact that the MIONet is very suitable for the proposed observer, since it is a very time-efficient discretization method and its moderate prediction error can be compensated for by the observer.

In order to assess the feasibility of implementing the proposed method in a real BMS, the computational resources required to perform a key BMS task (e.g., the online SOC estimation) were monitored. Within this paradigm, the integration of the two MIONets within the UKF observer gives rise to a state estimation process that encompasses supplementary operations intrinsic to the observer (cf. Eqs. (7)–(11)). Consequently, the computational time is inherently longer than that reported in Fig. 8, where only next state propagation was considered. The numerical tests were conducted on a machine equipped with an AMD Ryzen 9 7950X3D 16-core processor, with computation limited to a single core operating at 4.8 GHz. In a range of simulated scenarios, the estimation of the SOC required, on average, only 10 % of real-time execution. This indicates that the single core completed one hour of simulated operation in approximately six minutes. Among the main global microcontroller units (MCUs) suppliers, such as Infineon, NXP, Renesas, Texas Instruments, and STMicroelectronics, the typical clock speed of MCUs used in EVs/HEVs BMS applications ranges from 100 to 400 MHz, with RAM capacities of up to 10MB. The MCUs that demonstrate the highest levels of performance (for example, those with a frequency of 400 MHz) operate at approximately one-tenth the clock speed of the machine under investigation. Consequently, the observed computational efficiency indicates the potential of such MCUs to execute the SOC estimation in real time, under the assumption of comparable algorithmic and memory efficiency. With regard to the memory requirements, each MIONet is estimated to occupy approximately 750 kB of memory. Hence, the surrogate model has a total memory footprint of approximately 1.5 MB, which is well within the capacity of the RAM of the aforementioned MCUs, which typically provide several megabytes of memory. This finding suggests that the proposed approach is within the practical capabilities of contemporary BMS microcontroller hardware with respect to its computational and memory demands. It is also noteworthy that the implementation is written in Python, a high-level interpreted language that is not optimized for execution speed or memory efficiency. Conversely, the development of genuine BMS firmware is ordinarily executed in the programming languages C or C++, which offer considerably superior efficiency. Consequently, the performance measured with the Python-based prototype is likely to represent a conservative estimate, and further improvements in speed and memory usage are expected when the algorithm is migrated to an embedded environment using compiled languages.

### 3.4. Comparison with traditional online-state estimation approach

In this subsection, we compare the proposed method with the most widely used lumped-parameter model employed in model-based approaches for battery SOC estimation: the ECM [69–71]. The ECM represents the battery's electrical behavior using an equivalent electric circuit, while the SOC is calculated using the Coulomb counting method, which involves integrating the current drawn by the load. Despite its widespread use in online applications and its relatively simple parameterization, the ECM lacks detailed physical significance and only provides macro-level electrical quantities [6]. The ECM parameters, such as equivalent resistances, capacitances, and OCV, are typically determined through Hybrid Pulse Power Characterization (HPPC) tests and stored in look-up tables as functions of SOC [72–74]. The specific ECM considered in this study uses a Thevenin equivalent circuit. This circuit consists of an ideal voltage source representing the cell's equilibrium OCP as a function of SOC, a series resistance, and multiple RC branches connected in series. According to [71], increasing the number of RC branches can improve the approximation of battery dynamics, particularly under high current peaks, at the cost of increased model complexity. In our analysis, using more than three RC branches did not significantly improve the accuracy of the ECM's prediction, while unnecessarily increasing the complexity of the model. Thus, the considered ECM includes four states: three representing the polarization voltage across each RC branch and one for the SOC. The parameters of

the ECM model were estimated from the plant signal obtained by simulating an HPPC test, following the procedure described in Ref. [75]. The parameterized ECM is then integrated into a UKF for online state estimation. Similarly, the trained MIONet model is integrated into the UKF, but unlike the ECM, the MIONet uses 62 states, resulting from the spatial discretization of Li-ion concentration profiles into 31 radial points within each electrode, this being the best trade-off between computational cost and prediction accuracy observed in the analysis carried out in Section 3.3.

The filter parameters (i.e., the process and measurement noises) for both models are tuned to ensure high accuracy and precision in SOC estimation across all the scenarios studied. Moreover, both models are implemented with a sampling interval of one second ($\Delta t = 1s$). The plant is simulated using the full DFN model of a Li-ion battery, the state-of-the-art electrochemical model chosen to replicate realistic battery system dynamics. Simulated voltage observations are contaminated with Gaussian white measurement noise, characterized by a standard deviation of 1 mV. The battery current, which serves as the control input for the observer, is similarly affected by Gaussian white noise with a standard deviation of 1 mA. This simulation setup provides a controlled and repeatable environment to benchmark the proposed approach. In this study, DFN-generated synthetic data are used as a high-fidelity reference to evaluate the operator-learning framework as a model-order reduction technique and its integration into a model-based observer. In addition, we include a simple case study based on experimental data from the literature to provide an initial indication of real-world applicability. A comprehensive experimental validation, however, is beyond the scope of the present work and is left for future studies.

When considering electrochemical models, there are various definitions of SOC in the literature. All these definitions hinge on the quantity of Li-ions within the particle (the battery is considered “empty” when no more lithium atoms can release or collect electrons). However, some studies focus solely on the concentration of Li-ions on the particle surface, while others average the Li-ion concentrations across the entire radius of the representative electrode particle. We have observed that the former method is more suitable for low current intensities, whereas the latter, despite being computationally more expensive due to integration, provides a more comprehensive analysis. In this work, we adopt the latter approach, for which the SOC is computed as specified in Ref. [76]:

$$\bar{c}_{s,\mathrm{k}}(t) = \frac{\int_0^{R_\mathrm{k}} 4\pi r^2 c_{s,\mathrm{k}}(r,t)\, dr}{(4/3\ \pi {R_\mathrm{k}}^3)}, \quad \mathrm{k} \in \mathrm{n,p}$$

$$SOC_\mathrm{k}(t) = \frac{(\bar{c}_{s,\mathrm{k}}(t) - c_{s,\mathrm{k}}|_{SOC=0\ \%})}{(c_{s,\mathrm{k}}|_{SOC=100\ \%} - c_{s,\mathrm{k}}|_{SOC=0\ \%})}, \quad \mathrm{k} \in \mathrm{n,p}$$

$$SOC(t) = \frac{SOC_\mathrm{p}(t) + SOC_\mathrm{n}(t)}{2}$$

where $c_{s,\mathrm{k}}|_{SOC=100\ \%}$ and $c_{s,\mathrm{k}}|_{SOC=0\ \%}$ denote the mean Li-ion concentration values at 0 % SOC and 100 % in the respective electrodes.

Before comparing the proposed method against the ECM-based observer, we first introduce the two metrics used to evaluate their performance in terms of both accuracy and precision. Accuracy is assessed using the Root Mean Square Error (RMSE) of the state estimates, expressed as a percentage. Lower RMSE values indicate that the SOC estimates remain consistently close to the true values throughout the entire simulation horizon. Precision is assessed with the Coverage Width-based Criterion (CWC), a widely used metric that trades off coverage against sharpness by penalizing misses and discouraging unnecessary interval width [77]. The CWC score is defined as:

$$\mathrm{CWC} = \begin{cases} \mathrm{MPIW} \cdot (1 + \gamma \cdot \exp(-\eta \cdot (\mathrm{PICP} - \mu))), & \text{if PICP} < \mu \\ \mathrm{MPIW}, & \text{otherwise} \end{cases} \tag{14}$$

In Eq. (14) $\mathrm{MPIW} = \frac{1}{N}\sum_{i=1}^{N}(y_{\mathrm{upper},i} - y_{\mathrm{lower},i})$ is the mean prediction interval width; $\mathrm{PICP} = \frac{1}{N}\sum_{i=1}^{N} p\left\{y_{\mathrm{lower},i} \le y_i \le y_{\mathrm{upper},i}\right\}$ is the prediction interval coverage probability; $y$ is the estimated state mean value and $y_{\mathrm{lower}}$ and $y_{\mathrm{upper}}$ denote the lower and upper bounds of the 95 % confidence interval ($\pm 2\sigma$), respectively; $\mu$ is the target coverage level (e.g., 0.95); $\gamma$ is a penalty scaling factor; $\eta$ is a penalty sharpness factor. The CWC applies a penalty to the width if the actual coverage PICP falls below the desired threshold $\mu$, thus encouraging prediction intervals that are not only narrow but also reliable. In this work $\mu = 0.95$ is chosen to represent a 95 % confidence level, corresponding to a standard two-sigma interval under the assumption of normally distributed errors. The parameters $\eta = 1$ and $\gamma = 1$ are selected to apply a moderate penalty only when coverage is insufficient, avoiding excessive scaling of the penalty. A lower CWC score indicates a narrower and well-calibrated prediction interval, meaning the state estimate lies within the bounds with high probability. Conversely, a larger CWC score suggests overly wide intervals or that the true value frequently falls outside the confidence bounds, resulting in penalization.

#### 3.4.1. Performance comparison against different load current profiles

In order to assess the efficacy of the proposed methodology, the performance of the MIONet-based approach is compared to the ECM-based approach in several scenarios, considering different initial SOC values in the plant. These scenarios encompass a range of constant current charging conditions, from slow home charging to fast charging. As illustrated in Fig. 9(a), a comparative analysis of the charging performance between the two models is presented, showcasing a simulation of an ultra-slow home charging at 0.1 C-rate. Additionally, urban driving conditions are modeled using the UDDS drive cycle [78] scaled with various current intensities to simulate different EV/HEV driving scenarios. Fig. 9(b) presents a comparison of the two methods during a UDDS cycle whose maximum amplitude is scaled by 3 C-rate, for the modeled battery cell. A comprehensive summary of the comparison between the MIONet-based and ECM-based observers is provided in Table 2, which reports the SOC estimation accuracy and precision metrics computed across all scenarios tested. The SOC estimation performance obtained for ECM-based observers closely matches those reported in other works [69,70].

In all scenarios considered, the initial states are assumed to be unknown. A major advantage of integrating battery models into observers is their ability to estimate internal states without requiring prior knowledge of these initial conditions. The observer reconstructs the states using the measured output of the system, specifically the battery terminal voltage. However, it is important to recognize that accurate state estimation is not immediate; a convergence period is necessary, and its duration depends on the system dynamics as well as the measurement and process noise. In the early stages of estimation, the MIONet-based model exhibits slower convergence, particularly in terms of the state covariance, when compared to the ECM-based approach. This behavior stems from the inherently slower dynamics of the electrochemical model, in contrast to the faster-reacting dynamics of the ECM, which relies primarily on SOC estimation through Coulomb counting. Despite its slower convergence, the MIONet model achieves more stable and accurate SOC estimates during and after convergence. As illustrated in Fig. 9(a), corresponding to ultra-slow charging, the MIONet-based observer shows minimal fluctuations in SOC estimation. By contrast, the ECM is more susceptible to fluctuations induced by measurement noise in the current signal. This is due to its dependence on Coulomb counting, which accumulates error over time and amplifies the impact of noisy current measurements. Moreover, the slower dynamics of the electrochemical model prove advantageous in dynamic load conditions, such as those seen in the UDDS cycle. In Fig. 9(b), the ECM, which was parameterized using an HPPC cycle with 1 C-rate pulse discharges, demonstrates reduced accuracy when the current profile significantly deviates from its calibration experiment. While the ECM performs reliably under low-to-moderate currents, its accuracy deteriorates under high current loads, even when these occur in brief but sustained peaks, as is typical in UDDS cycles.

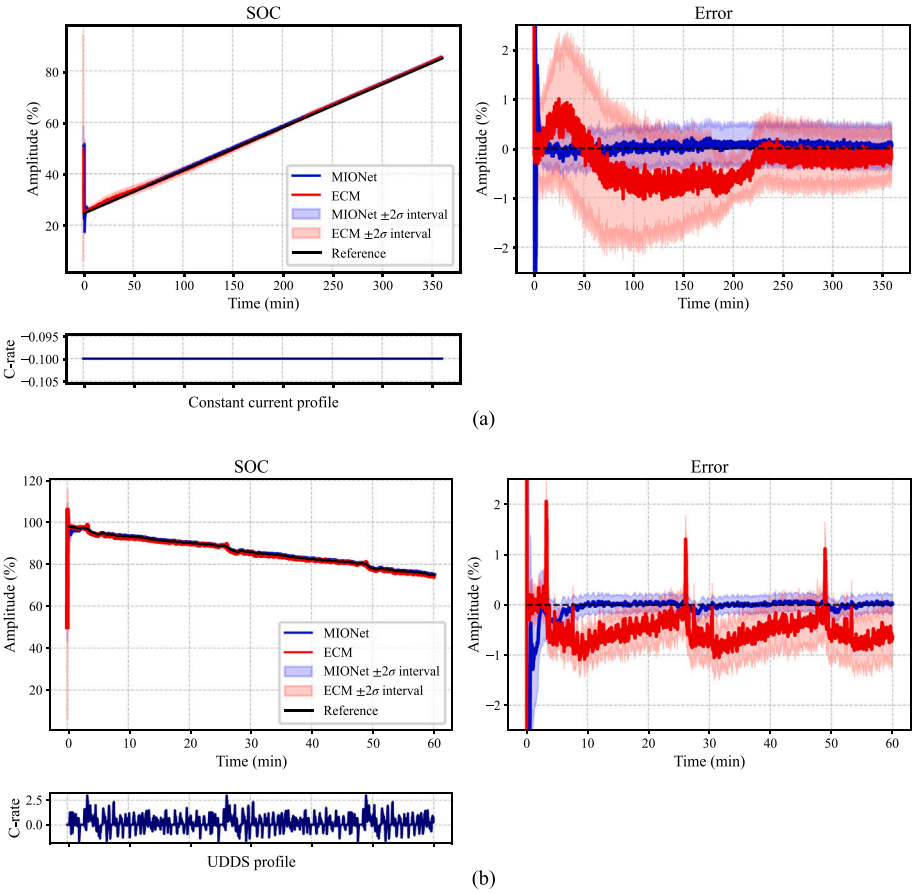


**Fig. 9.** SOC estimation comparison for the two methods. (a) Slow charging. (b) UDDS 2 cycle.

**Table 2**
Comparison of SOC estimation performance for the two tested methods under various simulated scenarios. The observer's estimation accuracy is evaluated using the RMSE between the estimated SOC and the true SOC, while estimation confidence is assessed using the CWC score (Eq. (14)). A lower CWC score indicates a more confident estimation. Best scores are indicated in green, worst scores in red.

| Scenario | Current peak (C-rate) | Duration (h) | RMSE SOC (%) | | CWC score | |
|---|---|---|---|---|---|---|
| | | | MIONet | ECM | MIONet | ECM |
| UDDS 1 | 1 | 2 | 0.058 | 0.18 | 0.63 | 1.2 |
| UDDS 2 | 3 | 1 | 0.044 | 0.25 | 0.60 | 3.7 |
| UDDS 3 | 5 | 1 | 0.25 | 2.1 | 2.1 | 4.2 |
| Ultra-slow charge | 0.1 | 6 | 0.063 | 0.49 | 0.83 | 3.4 |
| Slow charge | 0.2 | 4 | 0.079 | 0.34 | 1.0 | 1.5 |
| Moderate charge | 0.5 | 1.5 | 0.13 | 0.31 | 1.6 | 3.0 |
| Fast charge | 1 | 0.8 | 0.45 | 0.37 | 2.7 | 2.8 |

The MIONet-based observer, serving as a surrogate for the SPM within the UKF, exhibits some limitations when sustained operations at high C-rate are considered. This is an inherent shortcoming of the SPM, whose voltage formulation neglects lithium concentration dynamics and ohmic losses in the electrolyte. Consequently, under sustained high C-rate currents, the SPM tends to overestimate the cell voltage, introducing a systematic bias that can mislead the observer and impact state estimation accuracy. This limitation is already partially apparent in the fast-charging scenario, as reported in Table 2, where both the accuracy and precision of the MIONet-based estimator show the first signs of a noticeable drop. Nonetheless, its performance remains comparable to the ECM in this challenging regime. On the other hand, during dynamic profiles with short-duration high C-rate current peaks, such as in the UDDS case, the slower electrochemical dynamics of the SPM (diffusion and interfacial reaction processes) can partially compensate for the absence of electrolyte concentration effects, avoiding excessive overreaction to transient inputs. In these situations, the MIONet-based estimator maintains better consistency with the reference model and clearly outperforms the ECM, whose faster dynamics tend to overshoot under such conditions.

In conclusion, the results from Table 2 clearly indicate that the proposed SPM-based approach consistently outperforms the ECM in both accuracy and precision, with the sole exception of the fast charging case, where the performances are comparable, due to the aforementioned SPM limitations. The most evident advantage of the MIONet-based observer is observed in driving profiles that emulate real-world EV/HEV usage, particularly under dynamic traffic conditions, highlighting the ECM's key

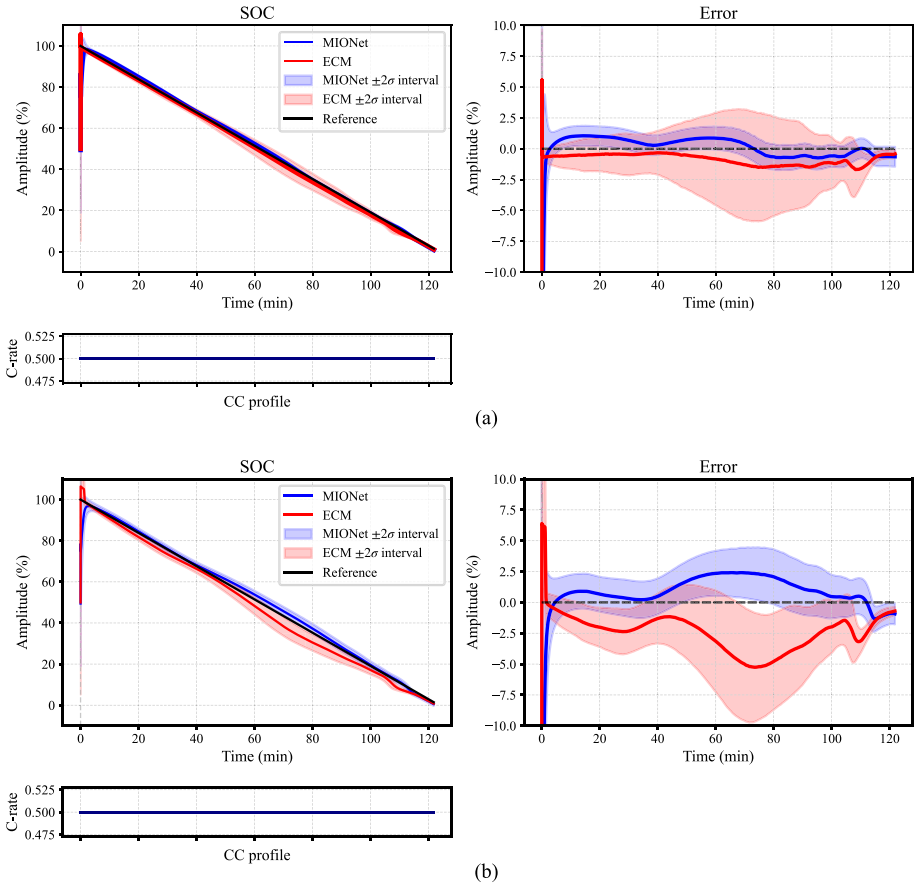


**Fig. 10.** SOC estimation comparison for the two methods. (a) Simulated plant. (b) Experimental plant.

limitation in such environments due to its reduced ability to capture internal battery physics.

### 3.4.2. Validation on experimental measurements

Up to this point, the proposed method has been validated using a plant based on the DFN model. This setup enabled validation of the two observers across a wide range of operating conditions, such as EV driving in traffic and during charging/discharging, but it relied on simulated measurements contaminated with white noise. To move closer to practical applications, we now validate the observers using experimental measurements obtained from a simple constant-discharge tests. This case approximates the observers operating directly on measurements from a physical battery system.

In this case study, the SPM parameters are based on the Enertech LCO-G SPB655060 commercially available pouch cell, taken from Ref. [79]. In that work, the authors report and make available experimental measurements of the terminal voltage for constant-current discharges at 2, 1 and 0.5 C-rate. The 2 C-rate case is considered out of the scope for this work, as it violates the underlying assumptions of the SPM. In fact, the SPM remains valid only under low current conditions or for short high-current pulses. Because the Enertech cell chemistry differs from that used in the previous case study, the two MIONets were retrained on the new parameter sets to learn the SPM equations associated with this chemistry, once again demonstrating the effectiveness of the method's transfer-learning capabilities. In practice, only limited retraining was needed, and the observers could be applied seamlessly to the new cell chemistry. For the same reason, the ECM was also re-parameterized for this chemistry following the standard HPPC-based procedure. To do so, a full DFN model of the Enertech cell was built in PyBaMM and used to simulate the HPPC test and extract the ECM parameters. This procedure ensures consistency in the comparison, although in practice the ECM would be parameterized by performing an HPPC test directly on the real battery cell. The need to rely on simulated HPPC data is therefore a limitation of this validation exercise. Moreover, Ref. [79] does not report SOC trajectories. To enable a comparison between the estimated SOC and a reference value, a simulation employing a DFN model is done to compute the concentration of lithium inside the battery's cell and consequently the "true" SOC. The 0.5 C-rate discharge results are shown in Fig. 10, with both cases (the observer validated against the simulated plant and against the experimental plant) plotted for visual comparison. Compared with the previous case study, both accuracy and precision are slightly worse due to the change in the parameter set. This new set, reflecting a different cell chemistry, features a flatter OCV–SOC curve. The reduced slope lowers the voltage sensitivity to SOC, which in turn amplifies uncertainty in the inferred state and especially degrades precision (wider confidence bands) while also making the estimates more susceptible to bias. A key feature of this validation is that the only measurement available from the experimental dataset is the terminal voltage. A direct comparison between the experimental voltage trace and the simulated plant voltage reveals smaller discrepancies, especially at mid-to-low SOC, caused by parameter uncertainty and unmodeled phenomena. As summarised in Table 3, these mismatches degrade both observers estimation performance. The ECM is particularly sensitive because it relies on accurate voltage reproduction and Coulomb counting. Consequently, its SOC estimates drift from the truth and exhibit greater uncertainty across discharge tests. In contrast, the MIONet-based observer is more tolerant of these discrepancies and maintains good estimation accuracy despite the voltage mismatch. This robustness comes from its electrochemical structure, which makes it less sensitive to measurement

**Table 3**
Comparison of SOC estimation performance for the two methods on both simulated and experimental datasets. The observer's estimation accuracy is evaluated using the RMSE between the estimated SOC and the true SOC, while estimation confidence is assessed using the CWC score (Eq. (14)). A lower CWC score indicates a more confident estimation. Best scores are indicated in green, worst scores in red.

| Scenario | C-rate | Plant | RMSE SOC (%) | | CWC score | |
|---|---|---|---|---|---|---|
| | | | MIONet | ECM | MIONet | ECM |
| Constant current discharge | 1 | Simulated | 0.88 | 0.56 | 6.2 | 8.5 |
| Constant current discharge | 1 | Experimental | 1.7 | 5.8 | 8.9 | 15 |
| Constant current discharge | 0.5 | Simulated | 0.70 | 0.97 | 4.4 | 9.6 |
| Constant current discharge | 0.5 | Experimental | 1.4 | 2.9 | 8.5 | 13.2 |

**Table 4**
Comparison of SOC estimation performance for the two methods under different ambient temperature considering scenario UDDS 2. The observer's estimation accuracy is evaluated using the RMSE between the estimated SOC and the true SOC, while estimation confidence is assessed using the CWC score (Eq. (14)). A lower CWC score indicates a more confident estimation. Best scores are indicated in green, and worst scores are indicated in red.

| Scenario | Current peak (C-rate) | Duration (h) | Ambient Temperature (°C) | RMSE SOC (%) | | CWC score | |
|---|---|---|---|---|---|---|---|
| | | | | MIONet | ECM | MIONet | ECM |
| UDDS 2 | 3 | 1 | 10 | 1.5 | 3.0 | 2.8 | 11 |
| UDDS 2 | 3 | 1 | 15 | 0.83 | 1.9 | 2.7 | 9.7 |
| UDDS 2 | 3 | 1 | 20 | 0.38 | 0.89 | 2.3 | 4.5 |
| UDDS 2 | 3 | 1 | 25 | 0.06 | 0.25 | 0.9 | 4.2 |
| UDDS 2 | 3 | 1 | 30 | 0.32 | 0.73 | 2.3 | 4.5 |
| UDDS 2 | 3 | 1 | 35 | 0.61 | 1.3 | 2.7 | 9.1 |
| UDDS 2 | 3 | 1 | 40 | 0.88 | 1.8 | 2.9 | 9.5 |

variability and moderate plant–model mismatch. Across the two discharges, MIONet consistently outperforms the ECM in both accuracy and precision. More broadly, these results reinforce a general principle: the more a model embeds physical structure, the wider the range of operating conditions over which it remains valid. We already observed this when the ECM-based observer was applied to highly dynamic scenarios (e.g., UDDS profiles). A similar pattern emerges here with experimental rather than simulated data. In practice, the performance of the ECM is closely related to the quality and representativeness of the tests used for its parameter identification, while physics-based surrogates such as MIONet exhibit greater transferability between cells and operating regimes.

Overall, these results confirm that while both approaches experience a performance drop compared to the purely simulated scenarios, the proposed MIONet-surrogate SPM observer demonstrates superior robustness when applied to experimental data. The reduced sensitivity to plant-model mismatches makes it a promising candidate for real-world BMS implementations, where uncertainties, unmodeled effects, and limited calibration opportunities are the norm. This experimental validation thus provides an important proof that the proposed method can be applied effectively to experimental measurements, moving beyond purely simulated benchmarks.

#### *3.4.3. Performance comparison at different ambient temperatures*

To assess the influence of temperature variations on the accuracy of the SOC estimation produced by the proposed method, we examined two scenarios. In the first, a lumped thermal model was incorporated into the DFN plant to account for self-heating due to electrochemical reactions. The SOC-estimation performance of the proposed observer was then re-evaluated using the UDDS 3 cycle and the fast-charging profile (i.e., two of the scenarios indicated in Table 2), both representative of high-current operating conditions. The results did not show significant differences between the SOC estimates obtained with and without thermal dynamics in the plant. In both cases, the average cell temperature increased by less than 3 °C, leading to negligible effects on the model dynamics, and both observers proved robust to such small thermal deviations.

In the second scenario, the plant ambient temperature was varied while the ECM and MIONet observers remained calibrated at the reference temperature of 25 °C, with no online thermal adaptation. Under these conditions, both observers exhibited an approximately constant offset in the SOC estimate, which became more pronounced as the ambient temperature deviated from the reference. This behavior can be attributed to the mismatch between the plant terminal voltage (corresponding to the actual cell temperature) and the predicted terminal voltage, which caused the observer to update the SOC based on a larger voltage residual.

For this scenario, we used the UDDS 2 cycle as the input current profile, and the SOC RMSE and CWC scores for different ambient temperatures are summarised in Table 4. The results indicate that MIONet is more stable across the tested temperature range, with a smaller increase in estimation error compared to the ECM, demonstrating improved robustness to thermal variations. This improved stability is likely due to the electrochemical model parameters being less sensitive to temperature changes than those estimated for the ECM.

## 4. Conclusions

This work presents a ROM for Li-ion batteries aimed at enhancing the accuracy and reliability of online state estimation using model-based approaches. To overcome the computational challenges associated with solving the system of PDEs in EMs, we propose a neural operator-based surrogate solver, namely, the MIONet. Trained with a purely physics-informed loss function, the MIONet learns the solution operator of the SPM without the need for labeled data or numerical solvers.

Compared to the approach proposed by Zheng et al. [53], this work introduces several improvements and advancements. First, initial concentration profiles are sampled from a GRF, and input current densities are drawn from a Gaussian distribution. This approach not only eliminates the need to solve the SPM when building the training database but also significantly improves the model's ability to generalize to unseen initial conditions and current inputs. As a result, MIONet accurately predicts concentration dynamics even under highly dynamic input profiles, such as UDDS load conditions.

Another notable advantage of the proposed framework lies in its generalizability across different battery chemistries. By adopting a non-dimensional formulation of the governing equations, the model captures the core diffusion behavior shared across battery types. This allows for efficient transfer learning, where a pre-trained MIONet can be fine-tuned on smaller, targeted datasets for new chemistries or geometries. Recent work by Subramanian et al. [80] confirms that transfer learning is particularly effective in physics-governed tasks, offering faster convergence and improved performance with significantly reduced data requirements. This is also demonstrated here, showing that minimal retraining of the MIONet is required when switching from an NMC cell to an LFP cell to achieve the same prediction accuracy of the concentration profiles.

Beyond accuracy and flexibility, computational efficiency is a critical requirement in BMSs, which often operate under strict real-time constraints. To address this, we compared MIONet with two established MOR techniques: OCFE and Padé approximation. Results show that MIONet outperforms both methods in terms of computational cost, offering a more scalable and efficient solution for real-time applications.

Leveraging the trained MIONet, we derive an explicit state-space representation of the battery's internal dynamics. This model is embedded within a UKF to perform real-time state estimation of key variables, such as the SOC. The proposed framework demonstrates the feasibility of integrating electrochemical models within observers while meeting low computational demands, which is promising for real-time operation. Validation across various load scenarios, including dynamic and high-rate charging conditions, as well as different ambient temperatures, confirms the robustness of this approach. Furthermore, simple experimental validation enhances the method's practical persuasiveness. Notably, this study provides the first comparative analysis between EM-based and ECM-based observers, highlighting the benefits of surrogate-assisted EMs for state estimation.

In summary, the main contributions of this work can be outlined as follows:

- Introduction of MIONet, a physics-informed neural operator surrogate for the SPM, trained without labeled data or numerical solvers.
- Use of GRF-sampled initial conditions and stochastic current profiles to enhance model generalization under dynamic load conditions.
- Generalizable non-dimensional formulation enabling efficient transfer learning across chemistries (e.g., NMC to LFP).
- Quantitative demonstration of computational efficiency, showing real-time capability and outperforming OCFE and Padé methods.
- Integration of the surrogate-based EM within a UKF for SOC estimation, validated against dynamic profiles and varying temperatures.
- First comparative analysis of EM-based and ECM-based observers, evidencing the benefits of surrogate-assisted EMs.

Although the SPM used in this study is not the most comprehensive electrochemical model, it provides accurate SOC estimates under current intensities up to 1 C. It also remains effective under dynamic loads with high current peaks due to the active material particles' inherently slow diffusion dynamics. However, the main limitation emerges in profiles with prolonged high C-rate operation. The absence of electrolyte concentration dynamics in the SPM leads to systematic voltage overestimation and consequently degraded estimation accuracy. To address this, the MIONet framework could be applied to more detailed models, such as the SPMe or DFN. These models can better capture the electrochemical behavior under sustained high currents by incorporating electrolyte transport effects and non-uniform reaction rate distributions, thereby mitigating the bias introduced by the SPM. However, these models' higher computational cost requires careful trade-off analysis between accuracy and complexity to ensure their suitability for real-time or embedded applications. This analysis could leverage MOR, adaptive model switching, or physics-informed surrogates to retain efficiency. Furthermore, this study focused on surrogating the SPM PDEs under isothermal conditions. However, the proposed framework can be extended to account for thermal dynamics to enhance prediction accuracy under varying environmental conditions. This can be achieved by incorporating temperature-dependent parameters into the operator network or coupling the electrochemical surrogate with an external thermal model. In practical BMS applications, tracking SOH is as critical as SOC, since SOH directly determines the remaining useful life and safe operating limits of the cell. The next logical step in this research is therefore to extend the proposed framework to SOH estimation and prediction. By augmenting the electrochemical model with degradation sub-models, such as SEI layer growth, lithium plating and active material loss, the operator-learning surrogate could capture the coupled evolution of capacity fade and resistance increase. Furthermore, integrating the surrogate model with sequential Bayesian filtering or probabilistic prognosis methods would facilitate real-time SOH estimation and forward-looking prediction of degradation trajectories under realistic operating conditions. This would allow both SOC and SOH to be estimated in real time within a unified, physics-informed framework, paving the way for predictive BMSs that can track current battery states and forecast long-term degradation trends. We foresee such an extension as part of our future research, as it would provide a more comprehensive and practical tool for advanced BMS applications.

## CRediT authorship contribution statement

**Lorenzo Brancato:** Writing – review & editing, Writing – original draft, Supervision, Software, Methodology, Conceptualization. **Alexander Gabriel Harej:** Writing – review & editing, Writing – original draft, Software, Methodology, Conceptualization. **Marco Giglio:** Supervision, Funding acquisition. **Francesco Cadini:** Writing – review & editing, Supervision, Conceptualization.

## Declaration of generative AI and AI-assisted technologies in the writing process

During the preparation of this work the authors used ChatGPT in order to improve clarity and readability in some critical parts. After using this tool, the authors reviewed and edited the content as needed and take full responsibility for the content of the publication.

## Declaration of competing interest

The authors declare that they have no known competing financial interests or personal relationships that could have appeared to influence the work reported in this paper.

## Acknowledgements

All source code and data used in this study are available at: https://github.com/HarejAl/Physics-informed-MIONet-for-Li-ion-battery-SOC-estimation/tree/main for reproducibility.

## Appendix A. Detailed DFN model formulation, nondimensionalisation, and asymptotic reduction to SPM

### A.1. Full dimensional DFN model

Li-on batteries are composed of two electrodes, a porous separator, an electrolyte, and two current collectors, as illustrated schematically in Fig. 1. Each electrode consists of active material particles within which lithium can be stored, and a binder that holds the electrode together and maintains an electrical connection between the active material particles and the current collectors.

Upon discharge, lithium intercalated in the negative electrode particles diffuses to the surface of the particles, where an electrochemical reaction occurs. This reaction produces a lithium ion free to move through the electrolyte and an electron free to move through the electrode. The electron travels through the electrode, into the current collector, through an external wire, and towards the positive electrode.

Concurrently, the lithium ion migrates through the electrolyte towards the positive electrode. At the surface of the positive electrode particles, the lithium ion and the electron combine through another electrochemical reaction to form a lithium atom intercalated in the positive electrode particle. To charge the battery, a voltage is applied across the cell, and the whole process occurs in reverse.

Here, the description of the DFN model is presented following the mathematical tractation employed in Ref. [27]. The latter model is the state-of-the-art electrochemical model of a Li-ion battery, offering a highly detailed and accurate representation of internal cell dynamics [13–15]. Throughout this section, we employ the superscript "*" to denote dimensional quantities. As illustrated in Fig. 1, the thicknesses of the negative electrode, separator, and positive electrode are denoted by $L_n^*$, $L_s^*$, and $L_p^*$, respectively. We denote the distance between the negative and positive current collectors by $L^* = L_n^* + L_s^* + L_p^*$. The active material particles in the negative and positive electrodes are assumed to be spheres with radii $R_n^*$ and $R_p^*$, respectively. Additionally, we assume that the behavior within each particle is spherically symmetric. We use the spatial coordinate $x^* \in [0, L^*]$ to indicate the location through the thickness of the battery and the spatial coordinate $r^* \in [0, R_k^*]$, $k \in \{n, p\}$ to indicate the location within each particle of active material. We define the following regions of the battery,

$$\Omega_n^* = [0, L_n^*], \quad \Omega_s^* = [L_n^*, L^* - L_p^*], \quad \Omega_p^* = [L^* - L_p^*, L^*]$$

which correspond to the negative electrode, separator, and positive electrode regions, respectively. We denote electric potentials by $\phi^*$, current densities by $i^*$, lithium concentrations by $c^*$ (in the electrolyte $c^*$ refer to Li-ion concentrations), and molar fluxes by $N^*$. To indicate the region within which each variable is defined, we include a subscript $k \in \{n, s, p\}$ which corresponds to $\Omega_n^*$, $\Omega_s^*$, and $\Omega_p^*$, respectively. To distinguish variables in the electrolyte from those in the solid phase of the electrode, we employ an additional subscript "e" for electrolyte variables and an additional subscript "s" for solid-phase variables. For clarity, the variables in the model and their corresponding regions are detailed hereafter:

$$\begin{aligned}
&\phi_{s,n}^*, \phi_{e,n}^*, c_{e,n}^*, i_{e,n}^*, N_{e,n}^* : && x^* \in \Omega_n^*,\\
&\phi_{e,s}^*, c_{e,s}^*, i_{e,s}^*, N_{e,s}^* : && x^* \in \Omega_s^*,\\
&\phi_{s,p}^*, \phi_{e,p}^*, c_{e,p}^*, i_{e,p}^*, N_{e,p}^* : && x^* \in \Omega_p^*,\\
&c_{s,n}^* : && r^* \in [0, R_n^*], \quad x^* \in \Omega_n^*,\\
&c_{s,p}^* : && r^* \in [0, R_p^*], \quad x^* \in \Omega_p^*.
\end{aligned}$$

We note that $c_{s,n}^*$ and $c_{s,p}^*$ depend on the macroscopic variable, $x^*$, the microscopic variable, $r^*$, and time, $t^*$, whereas all other variables depend on $x^*$ and $t^*$ only. When stating the governing equations, we take the region in which an equation holds to be implicitly defined by the subscript, $k \in \{n, s, p\}$, of the variables. With this notation in mind, the DFN model is summarised in Table A.5.

$U_n^*(c_{s,n}^*)$ and $U_p^*(c_{s,p}^*)$ represent the open-circuit potentials (OCPs) of the negative and positive electrodes, respectively, while $D_e^*(c_e^*)$ denotes the concentration-dependent diffusivity of Li-ions in the electrolyte. These functional forms were derived in the study by Mohtat et al. [65] by fitting experimental data on a graphite/NMC532 pouch cell. A complete list of model parameters and their corresponding values is provided in Table A.6, with all values sourced from Ref. [65]. The functions and parameters are specific to a Li-ion cell composed of a graphite negative electrode, a LiPF6 electrolyte, and a lithium nickel manganese cobalt (NMC) oxide positive electrode. Note that in Eq. (A.1e), (A.1d), and (A.1f) the actual current density $I^*$ is distinct from the typical current density $I_{typ}^*$ indicated in Table A.6.

### A.2. Nondimensionalisation

By following the asymptotic methods to reduce the DFN model used in Ref. [27], it is possible to obtain the SPM equations. In order to do this, it is first necessary to adimensionalize the DFN model with the following scaling:

$$\begin{aligned}
&\text{Global:} && x^* = L^* x, \quad t^* = \tau_d^* t, \quad D_e^* = D_{e,typ}^* D_e,\\
&&& \kappa_e^* = \kappa_{e,typ}^* \kappa_e, \quad I^* = I_{typ}^* I,\\
&&& \phi_{s,n}^* = \frac{R^*T^*}{F^*}\phi_{s,n}, \quad \phi_{s,p}^* = (U_{p,ref}^* - U_{n,ref}^*) + \frac{R^*T^*}{F^*}\phi_{s,p}.\\
&\text{For } k \in \{n, p\}: && r^* = R_k^* r_k, \quad c_{s,k}^* = c_{s,k,max}^* c_{s,k},\\
&&& j_k^* = \frac{I_{typ}^*}{a_k^* L^*} j_k, \quad j_{0,k}^* = \frac{I_{typ}^*}{a_k^* L^*} j_{0,k}, \quad m_k^* = m_{k,typ}^* m_k,\\
&&& \eta_k^* = \frac{R^*T^*}{F^*}\eta_k, \quad U_k^* = U_{k,ref}^* + \frac{R^*T^*}{F^*}U_k.\\
&\text{For } k \in \{n, p\}: && i_{s,k}^* = I_{typ}^* i_{s,k}.\\
&\text{For } k \in \{n, s, p\}: && c_{e,k}^* = c_{e,typ}^* c_{e,k}, \quad N_{e,k}^* = \frac{D_{e,typ}^* c_{e,typ}^*}{L^*} N_{e,k},\\
&&& \phi_{e,k}^* = -U_{n,ref}^* + \frac{R^*T^*}{F^*}\phi_{e,k}, \quad i_{e,k}^* = I_{typ}^* i_{e,k}.
\end{aligned} \tag{A.2}$$

Substituting the scaling (A.2) into the dimensional mathematical formulation of the DFN model described by Eq. (A.1a)–(A.1t) in Table A.5, we obtain the dimensionless version of the DFN model. The definition and the values of the time scales associated with the different physical processes are reported in Table A.7. The corresponding dimensionless parameters are summarised in Table A.8. Finally, Table A.9 summarises the dimensionless DFN model.

The expression for the terminal voltage in the adimensional formulation of the DFN model is

$$V = \phi_{s,p}|_{x=1} - \phi_{s,n}|_{x=0}. \tag{A.4}$$

It can be rewritten by decomposing a current path through the cell. Consider current entering at $x = 0$ through the negative solid, reacting at $x_n \in [0, L_n]$, traversing the electrolyte to $x_p \in [1 - L_p, 1]$, reacting again, and exiting through the positive solid. The voltage is:

$$\begin{aligned}
V = {} & \phi_{s,n}|_{x=x_n} - \phi_{s,n}|_{x=0} && \text{(Negative electrode)}\\
& + \phi_{e,n}|_{x=x_n} - \phi_{s,n}|_{x=x_n} && \text{(Negative electrochemical reaction)}\\
& + \phi_{e,p}|_{x=x_p} - \phi_{e,n}|_{x=x_n} && \text{(Electrolyte)}\\
& + \phi_{s,p}|_{x=x_p} - \phi_{e,p}|_{x=x_p} && \text{(Positive electrochemical reaction)}\\
& + \phi_{s,p}|_{x=1} - \phi_{s,p}|_{x=x_p} && \text{(Positive electrode)}
\end{aligned} \tag{A.5}$$

Defining the pointwise OCV

$$U_{eq}|_{x_n,x_p} = U_p(c_{s,p}|_{r=1})|_{x=x_p} - U_n(c_{s,n}|_{r=1})|_{x=x_n},$$

and the pointwise solid-phase Ohmic losses

$$\Delta\Phi_{Solid}|_{x_n,x_p} = (\phi_{s,p}|_{x=1} - \phi_{s,p}|_{x=x_p}) + (\phi_{s,n}|_{x=x_n} - \phi_{s,n}|_{x=0}),$$

and using Eq. (A.3q), we obtain

$$V = U_{eq}|_{x_n,x_p} + \eta_p|_{x=x_p} - \eta_n|_{x=x_n} + \phi_{e,p}|_{x=x_p} - \phi_{e,n}|_{x=x_n} + \Delta\Phi_{Solid}|_{x_n,x_p}. \tag{A.6}$$

### A.3. Asymptotic reduction to the SPM

We consider the limit of high electrical conductivity in electrodes and electrolyte and fast electrolyte transport, i.e., when $C_e \to 0$, $\sigma_k \to \infty$, and $\hat{\kappa}_e \to \infty$ with $\sigma_k C_e$ and $\hat{\kappa}_e C_e$ are constant:

$$\sigma_k = \frac{\sigma_k'}{C_e}, \quad \sigma_k' = \mathcal{O}(1), \quad k \in \{n, p\},$$

**Table A.5**
Mathematical description of the DFN model.

| **Governing equations** | | | **Boundary conditions** | | |
|---|---|---|---|---|---|
| *Charge conservation:* | | | *Current:* | | |
| $\frac{\partial i^*_{e,k}}{\partial x^*} = \begin{cases} a^*_k j^*_k, & k = n, p \\ 0, & k = s \end{cases}$ | | (A.1a) | $i^*_{e,n}\|_{x^*=0} = i^*_{e,p}\|_{x^*=L^*} = 0,$ | | (A.1b) |
| $i^*_{e,k} = \epsilon^b_k \kappa^*_e(c^*_{e,k})\left(-\frac{\partial \phi^*_{e,k}}{\partial x^*} + 2(1-t^+)\frac{R^*T^*}{F^*}\frac{\partial}{\partial x^*}\left(\log\left(c^*_{e,k}\right)\right)\right)$ | $k \in \{n, s, p\}$ | (A.1c) | $\phi^*_{e,n}\|_{x^*=L^*_n} = \phi^*_{e,s}\|_{x^*=L^*_n}, \quad i^*_{e,n}\|_{x^*=L^*_n} = i^*_{e,s}\|_{x^*=L^*_n} = I^*$ | | (A.1d) |
| $I^* - i^*_{e,k} = -\sigma^*_k \frac{\partial \phi^*_{s,k}}{\partial x^*},$ | $k \in \{n, p\}$ | (A.1e) | $\phi^*_{e,s}\|_{x^*=L^*-L^*_p} = \phi^*_{e,p}\|_{x^*=L^*-L^*_p}, \quad i^*_{e,s}\|_{x^*=L^*-L^*_p} = i^*_{e,p}\|_{x^*=L^*-L^*_p} = I^*$ | | (A.1f) |
| *Molar conservation:* | | | *Concentration in electrolyte:* | | |
| $\epsilon_k \frac{\partial c^*_{e,k}}{\partial t^*} = \frac{\partial N^*_{e,k}}{\partial x^*} + \frac{1}{F^*}\frac{\partial i^*_{e,k}}{\partial x^*},$ | $k \in \{n, s, p\}$ | (A.1g) | $N^*_{e,n}\|_{x^*=0} = N^*_{e,p}\|_{x^*=L^*} = 0,$ | | (A.1h) |
| $N^*_{e,k} = \epsilon^b_k D^*_e(c^*_{e,k})\frac{\partial c^*_{e,k}}{\partial x^*} + \frac{t^+}{F} i^*_{e,k},$ | $k \in \{n, s, p\}$ | (A.1i) | $c^*_{e,n}\|_{x^*=L^*_n} = c^*_{e,s}\|_{x^*=L^*_n}, \quad N^*_{e,n}\|_{x^*=L^*_n} = N^*_{e,s}\|_{x^*=L^*_n}$ | | (A.1j) |
| $\frac{\partial c^*_{s,k}}{\partial t^*} = \frac{1}{(r^*)^2}\frac{\partial}{\partial r^*}\left((r^*)^2 D^*_{s,k}\frac{\partial c^*_{s,k}}{\partial r^*}\right),$ | $k \in \{n, p\}$ | (A.1k) | $c^*_{e,s}\|_{x^*=L^*-L^*_p} = c^*_{e,p}\|_{x^*=L^*-L^*_p}, \quad N^*_{e,s}\|_{x^*=L^*-L^*_p} = N^*_{e,p}\|_{x^*=L^*-L^*_p}$ | | (A.1l) |
| *Electrochemical reactions:* | | | *Concentration in electrode material:* | | |
| $j^*_k = j^*_{0,k}\sinh\left(\frac{F^*\eta^*_k}{2\,R^*T^*}\right),$ | $k \in \{n, p\}$ | (A.1m) | $\frac{\partial c^*_{s,k}}{\partial r^*}\|_{r^*=0} = 0,$ | $k \in \{n, p\}$ | (A.1n) |
| $j^*_{0,k} = m^*_k (c^*_{s,k})^{1/2}(c^*_{s,k,max} - c^*_{s,k})^{1/2}(c^*_{e,k})^{1/2},$ | $k \in \{n, p\}$ | (A.1o) | $-D_{s,k}\frac{\partial c^*_{s,k}}{\partial r^*}\|_{r^*=R^*_k} = \frac{j^*_k}{F^*},$ | $k \in \{n, p\}$ | (A.1p) |
| $\eta^*_k = \phi^*_{s,k} - \phi^*_{e,k} - U_k(c^*_{s,k}\|_{r^*=R^*_k}),$ | $k \in \{n, p\}$ | (A.1q) | | | |
| **Reference potential** | | | **Initial conditions** | | |
| $\phi^*_{s,n}\|_{x^*=0} = 0$ | | (A.1r) | $c^*_{s,k}(x^*, r^*, 0) = c^*_{s,k,0},$ | $k \in \{n, p\}$ | (A.1s) |
| | | | $c^*_{e,k}(x^*, 0) = c^*_{e,typ},$ | $k \in \{n, s, p\}$ | (A.1t) |

**Table A.6**
Dimensional model parameters with values taken from Ref. [65].

| Parameters | Units | Description | $\Omega^*_n$ | $\Omega^*_s$ | $\Omega^*_p$ |
|---|---|---|---|---|---|
| $\epsilon_k$ | – | Electrolyte volume fraction | 0.61 | 1 | 0.445 |
| $c^*_{k,max}$ | $mol/m^3$ | Maximum lithium concentration | $2.8746 \times 10^4$ | – | $3.5380 \times 10^4$ |
| $\sigma^*_k$ | S/m | Solid conductivity | 100 | – | 100 |
| $D^*_{s,k}$ | $m^2/s$ | Electrode diffusivity | $5 \times 10^{-15}$ | – | $8 \times 10^{-15}$ |
| $R^*_k$ | $\mu$m | Particle radius | 2.5 | – | 3.5 |
| $a^*_k$ | $\mu m^{-1}$ | Electrode surface area density | 0.732 | – | 0.381 |
| $m^*_k$ | $(A/m^2)(m^3/mol)^{1.5}$ | Reaction rate | $1.061 \times 10^{-6}$ | – | $4.824 \times 10^{-6}$ |
| $L^*_k$ | $\mu$m | Thickness | 62 | 12 | 67 |
| $U^*_{k,ref}$ | V | Reference potential | 0.18 | – | 3.94 |
| $c^*_{e,typ}$ | $mol/m^3$ | Typical lithium concentration in electrolyte | | $1 \times 10^3$ | |
| $D^*_{e,typ}$ | $m^2/s$ | Typical electrolyte diffusivity | | $5.35 \times 10^{-10}$ | |
| $\kappa^*_{e,typ}$ | S/m | Typical electrolyte conductivity | | 1.3 | |
| $F^*$ | C/mol | Faraday's constant | | 96485 | |
| $R^*$ | J/(mol K) | Universal gas constant | | 8.314472 | |
| $T^*$ | K | Temperature | | 298.15 | |
| $b$ | – | Bruggerman coefficient | | 1.5 | |
| $t^+$ | – | Transference number | | 0.38 | |
| $I^*_{typ}$ | $A/m^2$ | Typical current density | | 24.4 (1C) | |

**Table A.7**
Time scales associated with the physical processes occurring within the battery cell model. Here $C = I^*/(24.4 A m^{-2})$ is the cell C-rate (assuming 1 C corresponds to 24.4 A $m^{-2}$).

| Symbol | Expression | Interpretation | Values [s] |
|---|---|---|---|
| $\tau^*_d$ | $F^* c^*_{n,max} L^*/I^*_{typ}$ | Discharge timescale | $1.603 \times 10^4/C$ |
| $\tau^*_n$ | $(R^*_n)^2/D^*_{s,n}$ | Diffusion timescale in the negative electrode particle | $1.250 \times 10^3$ |
| $\tau^*_p$ | $(R^*_p)^2/D^*_{s,p}$ | Diffusion timescale in the positive electrode particle | $1.531 \times 10^3$ |
| $\tau^*_e$ | $(L^*)^2/D^*_{e,typ}$ | Diffusion timescale in electrolyte | 37.16 |
| $\tau^*_{r,n}$ | $F^*/(m^*_n a^*_n (c^*_{e,typ})^{1/2})$ | Reaction timescale in the negative electrode | $3.929 \times 10^3$ |
| $\tau^*_{r,p}$ | $F^*/(m^*_p a^*_p (c^*_{e,typ})^{1/2})$ | Reaction timescale in the positive electrode | $3.166 \times 10^3$ |

$$\hat{\kappa}_e = \frac{\hat{\kappa}'_e}{C_e}, \quad \hat{\kappa}'_e = \mathcal{O}(1).$$

We expand variables in powers of $C_e$:

$$c_{s,k} \approx c^0_{s,k} + C_e c^1_{s,k} + C_e^2 c^2_{s,k} + \dots$$

At leading order, the electrolyte potential drop and solid-phase Ohmic losses vanish, yielding the SPM in Table A.10. This approximation is valid when the electrolyte migration timescale is much shorter than the discharge timescale (typically for low-current applications).

At leading order, $c^0_{s,k}$ is independent of $x$, thus the electrode-averaged OCV is

$$\bar{U}^0_{eq} = \bar{U}_p(c^0_{s,p}|_{r=1}) - \bar{U}_n(c^0_{s,n}|_{r=1}),$$

and the leading-order electrode-averaged reaction overpotentials satisfy $\bar{\eta}^0_k = \eta^0_k$, yielding Eq. (1) with $j^0_{0,k} = \frac{\gamma_k}{C_{r,k}}(c_{s,k})^{1/2}(1 - c_{s,k})^{1/2}$.

**Table A.8**
Adimensional DFN model parameters. Here, $C$ is the cell C-rate.

| Parameter | Expression | Interpretation | n | s | p |
|---|---|---|---|---|---|
| $L_k$ | $L_k^*/L^*$ | Ratio of region thickness to cell thickness | 0.4397 | 0.0851 | 0.4752 |
| $C_k$ | $\tau_k^*/\tau_d^*$ | Ratio of solid diffusion and discharge timescales | 0.0780 $C$ | – | 0.0995 $C$ |
| $C_{r,k}$ | $\tau_{r,k}^*/\tau_d^*$ | Ratio of reaction and discharge timescales | 0.2451 $C$ | – | 0.1038 $C$ |
| $\sigma_k$ | $(R^*T^*/F^*)/(I_{typ}^*L^*/\sigma_k^*)$ | Ratio of thermal voltage to typical solid Ohmic drop | $746.8/C$ | – | $746.8/C$ |
| $a_k$ | $a_k^*R_k^*$ | Product of particle radius and surface area density | 1.83 | – | 1.33 |
| $\gamma_k$ | $c_{k,max}^*/c_{n,max}^*$ | Ratio of max solid concentrations | 1 | – | 1.2308 |
| $C_e$ | $\tau_e^*/\tau_d^*$ | Ratio of electrolyte transport and discharge timescales | | $2.32\times10^{-3}C$ | |
| $\gamma_e$ | $c_{e,typ}^*/c_{n,max}^*$ | Ratio of typical electrolyte to max solid concentration | | 0.035 | |
| $\hat{\kappa}_e$ | $(R^*T^*/F^*)/(I_{typ}^*L^*/\hat{\kappa}_e^*)$ | Thermal voltage to typical electrolyte Ohmic drop | | $9.708/C$ | |
| $c_{k,0}$ | $c_{k,0}^*/c_{k,max}^*$ | Ratio of initial to max solid concentration | 0.0017 | – | 0.8907 |

**Table A.9**
Adimensional mathematical description of the DFN model.

| Governing equations | | | Boundary conditions | | |
|---|---|---|---|---|---|
| *Charge conservation:* | | | *Current:* | | |
| $\frac{\partial i_{e,k}}{\partial x} = \begin{cases} j_k, & k = n, p \\ 0, & k = s \end{cases}$ | | (A.3a) | $i_{e,n}\|_{x=0} = i_{e,p}\|_{x=1} = 0,$ | | (A.3b) |
| $i_{e,k} = \epsilon_k^b \hat{\kappa}_e \kappa_e(c_{e,k})\left(-\frac{\partial \phi_{e,k}}{\partial x} + 2(1-t^+)\frac{\partial}{\partial x}\left(\log\left(c_{e,k}\right)\right)\right),$ | $k \in \{n, s, p\}$ | (A.3c) | $\phi_{e,n}\|_{x=L_n} = \phi_{e,s}\|_{x=L_n}, \quad i_{e,n}\|_{x=L_n} = i_{e,s}\|_{x=L_n} = I,$ | | (A.3d) |
| $I - i_{e,k} = -\sigma_k \frac{\partial \phi_{s,k}}{\partial x},$ | $k \in \{n, p\}$ | (A.3e) | $\phi_{e,s}\|_{x=1-L_p} = \phi_{e,p}\|_{x=1-L_p}, \quad i_{e,s}\|_{x=1-L_p} = i_{e,p}\|_{x=1-L_p} = I,$ | | (A.3f) |
| *Molar conservation:* | | | *Concentration in electrolyte:* | | |
| $C_e \epsilon_k \gamma_e \frac{\partial c_{e,k}}{\partial t} = -\gamma_e \frac{\partial N_{e,k}}{\partial x} + C_e \frac{\partial i_{e,k}}{\partial x},$ | $k \in \{n, s, p\}$ | (A.3g) | $N_{e,n}\|_{x=0} = N_{e,p}\|_{x=1} = 0,$ | | (A.3h) |
| $N_{e,k} = -\epsilon_k^b D_e(c_{e,k})\frac{\partial c_{e,k}}{\partial x} + \frac{C_e t^+}{\gamma_e} i_{e,k},$ | $k \in \{n, s, p\}$ | (A.3i) | $c_{e,n}\|_{x=L_n} = c_{e,s}\|_{x=L_n}, \quad N_{e,n}\|_{x=L_n} = N_{e,s}\|_{x=L_n},$ | | (A.3j) |
| $C_k \frac{\partial c_{s,k}}{\partial t} = \frac{1}{r_k^2}\frac{\partial}{\partial r_k}\left(r_k^2 \frac{\partial c_{s,k}}{\partial r_k}\right),$ | $k \in \{n, p\}$ | (A.3k) | $c_{e,s}\|_{x=1-L_p} = c_{e,p}\|_{x=1-L_p}, \quad N_{e,s}\|_{x=1-L_p} = N_{e,p}\|_{x=1-L_p}$ | | (A.3l) |
| *Electrochemical reactions:* | | | *Concentration in electrode material:* | | |
| $j_k = j_{0,k}\sinh\left(\frac{\eta_k}{2}\right),$ | $k \in \{n, p\}$ | (A.3m) | $\frac{\partial c_{s,k}}{\partial r_k}\|_{r=0} = 0,$ | $k \in \{n, p\}$ | (A.3n) |
| $j_{0,k} = \frac{\gamma_k}{C_{r,k}}(c_{s,k})^{1/2}(1-c_{s,k})^{1/2}(c_{e,k})^{1/2}\|_{r_k=1},$ | $k \in \{n, p\}$ | (A.3o) | $-\frac{a_k\gamma_k}{C_k}\frac{\partial c_{s,k}}{\partial r_k}\|_{r_k=1} = j_k,$ | $k \in \{n, p\}$ | (A.3p) |
| $\eta_k = \phi_{s,k} - \phi_{e,k} - U_k(c_{s,k}\|_{r_k=1}),$ | $k \in \{n, p\}$ | (A.3q) | | | |
| **Reference potential** | | | **Initial conditions** | | |
| $\phi_{s,n}\|_{x=0} = 0$ | | (A.3r) | $c_{s,k}(x, r_k, 0) = c_{s,k,0},$ | $k \in \{n, p\}$ | (A.3s) |
| | | | $c_{e,k}(x, 0) = 1,$ | $k \in \{n, s, p\}$ | (A.3t) |

**Table A.10**
Mathematical adimensional description of the SPM model.

| | | |
|---|---|---|
| **Governing equations** | | |
| *Charge conservation:* | | |
| $C_k \frac{\partial c_{s,k}^0}{\partial t} = \frac{1}{r_k^2}\frac{\partial}{\partial r_k}\left(r_k^2 \frac{\partial c_{s,k}^0}{\partial r_k}\right),$ | $k \in \{n, p\}.$ | (A.7a) |
| **Boundary conditions** | | |
| *Concentration in the electrode active material:* | | |
| $\frac{\partial c_{s,k}^0}{\partial r_k}\|_{r=0} = 0,$ | $k \in \{n, p\},$ | (A.7b) |
| $-\frac{a_k\gamma_k}{C_k}\frac{\partial c_{s,k}^0}{\partial r_k}\|_{r_k=1} = \begin{cases} \frac{I}{L_n}, & k = n, \\ -\frac{I}{L_p} & k = p, \end{cases}$ | $k \in \{n, p\},$ | (A.7c) |
| **Initial conditions** | | |
| $c_{s,k}^0(x, r_k, 0) = c_{s,k,0},$ | $k \in \{n, p\},$ | (A.7d) |

## Data availability

Data will be made available on request.

## References


[1] Alanazi F. Electric vehicles: benefits, challenges, and potential solutions for widespread adaptation. Appl Sci 2023;13(10). https://doi.org/10.3390/app13106016. https://www.mdpi.com/2076-3417/13/10/6016.

[2] Pamidimukkala A, Kermanshachi S, Rosenberger JM, Hladik G. Barriers and motivators to the adoption of electric vehicles: a global review. Green Energy Intell Transp 2024;3(2):100153. https://doi.org/10.1016/j.geits.2024.100153

[3] Scrosati B, Garche J. Lithium batteries: status, prospects and future. J Power Sources 2010;195(9):2419–30. https://doi.org/10.1016/j.jpowsour.2009.11.048

[4] Scrosati B, Hassoun J, Sun Y-K. Lithium-ion batteries. A look into the future. Energy Environ Sci 2011;4(9):3287–95. https://doi.org/10.1039/C1EE01388B

[5] Li J, Du Z, Ruther RE, An SJ, David LA, Hays K, Wood M, Phillip ND, Sheng Y, Mao C, et al. Toward low-cost, high-energy density, and high-power density lithium-ion batteries. Jom 2017;69:1484–96.

[6] Hu X, Xu L, Lin X, Pecht M. Battery lifetime prognostics. Joule 2020;4(2):310–46.

[7] Gu R, Malysz P, Yang H, Emadi A. On the suitability of electrochemical-based modeling for lithium-ion batteries. IEEE Trans Transp Electrific 2016;2(4):417–31.

[8] Krewer U, Röder F, Harinath E, Braatz RD, Bedürftig B, Findeisen R. Dynamic models of li-ion batteries for diagnosis and operation: a review and perspective. J Electrochem Soc 2018;165(16):A3656.

[9] Seaman A, Dao T-S, McPhee J. A survey of mathematics-based equivalent-circuit and electrochemical battery models for hybrid and electric vehicle simulation. J Power Sources 2014;256:410–23.

[10] Sun L, Li G, You F. Combined internal resistance and state-of-charge estimation of lithium-ion battery based on extended state observer. Renew Sustain Energy Rev 2020;131:109994.

[11] Chaturvedi NA, Klein R, Christensen J, Ahmed J, Kojic A. Algorithms for advanced battery-management systems. IEEE Control Syst Mag 2010;30(3):49–68.

[12] Kolluri S, Aduru SV, Pathak M, Braatz RD, Subramanian VR. Real-time nonlinear model predictive control (nmpc) strategies using physics-based models for advanced lithium-ion battery management system (bms). J Electrochem Soc 2020;167(6):063505.

[13] Doyle M, Fuller TF, Newman J. Modeling of galvanostatic charge and discharge of the lithium/polymer/insertion cell. J Electrochem Soc 1993;140(6):1526.

[14] Fuller TF, Doyle M, Newman J. Simulation and optimization of the dual lithium ion insertion cell. J Electrochem Soc 1994;141(1):1.

[15] Doyle M, Newman J. Modeling the performance of rechargeable lithium-based cells: design correlations for limiting cases. J Power Sources 1995;54(1):46–51.

[16] Subramanian VR, Boovaragavan V, Ramadesigan V, Arabandi M. Mathematical model reformulation for lithium-ion battery simulations: Galvanostatic boundary conditions. J Electrochem Soc 2009;156(4):A260.

[17] Safari M, Delacourt C. Modeling of a commercial graphite/lifepo4 cell. J Electrochem Soc 2011;158(5):A562.

[18] Guo M, White RE. A distributed thermal model for a li-ion electrode plate pair. J Power Sources 2013;221:334–44.

[19] Sturm J, Ludwig S, Zwirner J, Ramirez-Garcia C, Heinrich B, Horsche MF, Jossen A. Suitability of physicochemical models for embedded systems regarding a nickel-rich, silicon-graphite lithium-ion battery. J Power Sources 2019;436:226834.

[20] Reniers JM, Mulder G, Howey DA. Review and performance comparison of Mechanical-chemical degradation models for lithium-ion batteries. J Electrochem Soc 2019;166(14):3189–200.

[21] Smith KA, Rahn CD, Wang C-Y. Control oriented 1d electrochemical model of lithium ion battery. Energy Convers Manag 2007;48(9):2565–78.

[22] Allam A, Onori S. Online capacity estimation for lithium-ion battery cells via an electrochemical model-based adaptive interconnected observer. IEEE Trans Control Syst Technol 2020;29(4):1636–51.

[23] Gima ZT, Kato D, Klein R, Moura SJ. Analysis of online parameter estimation for electrochemical li-ion battery models via reduced sensitivity equations. In: 2020 American Control Conference (ACC); IEEE; 2020. p. 373–8.

[24] Rahman MA, Anwar S, Izadian A. Electrochemical model based fault diagnosis of a lithium ion battery using multiple model adaptive estimation approach. In: 2015 IEEE International Conference on Industrial Technology (ICIT); IEEE; 2015. p. 210–7.

[25] Li Y, Karunathilake D, Vilathgamuwa DM, Mishra Y, Farrell TW, Zou C, et al. Model order reduction techniques for physics-based lithium-ion battery management: a survey. IEEE Ind Electron Mag 2021;16(3):36–51.

[26] Santhanagopalan S, Guo Q, Ramadass P, White RE. Review of models for predicting the cycling performance of lithium ion batteries. J Power Sources 2006;156(2):620–8.

[27] Marquis SG, Sulzer V, Timms R, Please CP, Chapman SJ. An asymptotic derivation of a single particle model with electrolyte. J Electrochem Soc 2019;166(15):A3693.

[28] Li W, Fan Y, Ringbeck F, Jöst D, Han X, Ouyang M, Sauer DU. Electrochemical model-based state estimation for lithium-ion batteries with adaptive unscented Kalman filter. J Power Sources 2020;476:228534.

[29] Marelli S, Corno M. Model-based estimation of lithium concentrations and temperature in batteries using soft-constrained dual unscented Kalman filtering. IEEE Trans Control Syst Technol 2020;29(2):926–33.

[30] Dey S, Ayalew B, Pisu P. Nonlinear robust observers for state-of-charge estimation of lithium-ion cells based on a reduced electrochemical model. IEEE Trans Control Syst Technol 2015;23(5):1935–42.

[31] Li Y, Xiong B, Vilathgamuwa DM, Wei Z, Xie C, Zou C. Constrained ensemble Kalman filter for distributed electrochemical state estimation of lithium-ion batteries. IEEE Trans Ind Informatics 2020;17(1):240–50.

[32] Bizeray AM, Zhao S, Duncan SR, Howey DA. Lithium-ion battery thermal-electrochemical model-based state estimation using orthogonal collocation and a modified extended Kalman filter. J Power Sources 2015;296:400–12.

[33] Rodríguez A, Plett GL, Trimboli MS. Improved transfer functions modeling linearized lithium-ion battery-cell internal electrochemical variables. J Energy Storage 2018;20:560–75.

[34] Zhang R, Xia B, Li B, Cao L, Lai Y, Zheng W, Wang H, Wang W. State of the art of lithium-ion battery soc estimation for electrical vehicles. Energies 2018;11(7).

[35] Xia B, Cui D, Sun Z, Lao Z, Zhang R, Wang W, Sun W, Lai Y, Wang M. State of charge estimation of lithium-ion batteries using optimized levenberg-marquardt wavelet neural network. Energy 2018;153:694–705.

[36] Dang X, Yan L, Xu K, Wu X, Jiang H, Sun H. Open-circuit voltage-based state of charge estimation of lithium-ion battery using dual neural network fusion battery model. Electrochim Acta 2016;188:356–66.

[37] Tong S, Lacap JH, Park JW. Battery state of charge estimation using a load-classifying neural network. J Energy Storage 2016;7:236–43.

[38] Yang N, Song Z, Hofmann H, Sun J. Robust state of health estimation of lithium-ion batteries using convolutional neural network and random forest. J Energy Storage 2022;48:103857. https://doi.org/10.1016/j.est.2021.103857

[39] Chaoui H, Ibe-Ekeocha CC. State of charge and state of health estimation for lithium batteries using recurrent neural networks. IEEE Trans Vehicular Technol 2017;66(10):8773–83. https://doi.org/10.1109/TVT.2017.2715333

[40] Yang D, Wang Y, Pan R, Chen R, Chen Z. A neural network based state-of-health estimation of lithium-ion battery in electric vehicles. Energy Procedia 2017;105:2059–64.

[41] Hornik K, Stinchcombe M, White H. Multilayer feedforward networks are universal approximators. Neural Netw 1989;2(5):359–66.

[42] Chen T, Chen H. Approximations of continuous functionals by neural networks with application to dynamic systems. IEEE Trans Neural Netw 1993;4(6):910–8.

[43] Chen T, Chen H. Universal approximation to nonlinear operators by neural networks with arbitrary activation functions and its application to dynamical systems. IEEE Trans Neural Netw 1995;6(4):911–7.

[44] Lu L, Jin P, Pang G, Zhang Z, Karniadakis GE. Learning nonlinear operators via deeponet based on the universal approximation theorem of operators. Nat Mach Intell 2021;3(3):218–29.

[45] Wang S, Wang H, Perdikaris P. Learning the solution operator of parametric partial differential equations with physics-informed deeponets. Sci Adv 2021;7(40):eabi8605.

[46] Jin P, Meng S, Lu L. Mionet: learning multiple-input operators via tensor product. SIAM J Sci Comput 2022;44(6):3490–514.

[47] Tu H, Moura S, Wang Y, Fang H. Integrating physics-based modeling with machine learning for lithium-ion batteries. Appl Energy 2023;329:120289.

[48] Borah M, Wang Q, Moura S, Sauer DU, Li W. Synergizing physics and machine learning for advanced battery management. Commun Eng 2024;3(1):134.

[49] Wang F, Zhai Z, Zhao Z, Di Y, Chen X. Physics-informed neural network for lithium-ion battery degradation stable modeling and prognosis. Nat Commun 2024;15(1):4332.

[50] Amiri MN, Håkansson AEM, Burheim OS, Lamb JJ. Lithium-ion battery digitalization: combining physics-based models and machine learning. Renew Sustain Energy Rev 2024;200:114577.

[51] Sapra HD, Elfimova O, Upadhya S, Desorcy L, Wagner M, Venkataraman S, Kweon C-B, Kokjohn S, Shumaker J. Estimating battery state-of-charge using machine learning and physics-based models, Tech. rep., SAE Technical Paper; 2023.

[52] Finegan DP, Zhu J, Feng X, Keyser M, Ulmefors M, Li W, Bazant MZ, Cooper SJ. The application of data-driven methods and physics-based learning for improving battery safety. Joule 2021;5(2):316–29.

[53] Zheng Q, Yin X, Zhang D. State-space modeling for electrochemical performance of li-ion batteries with physics-informed deep operator networks. J Energy Storage 2023;73:109244.

[54] Wang S, Wang H, Perdikaris P. Learning the solution operator of parametric partial differential equations with physics-informed deeponets. Sci Adv 2021;7.

[55] Sulzer V, Marquis SG, Timms R, Robinson M, Chapman SJ. Python battery mathematical modelling (pybamm). J Open Res Softw 2021;9(1).

[56] Jin P, Meng S, Lu L. Mionet: learning multiple-input operators via tensor product. SIAM J Sci Comput 2022.

[57] Kalman RE. A new approach to linear filtering and prediction problems. J Basic Eng 1960;82:35–45.

[58] Smith GL, Schmidt SF, McGee LA. Application of statistical filter theory to the optimal estimation of position and velocity on board a circumlunar vehicle, vol. 135. National Aeronautics and Space Administration; 1962.

[59] Julier SJ. The scaled unscented transformation. In: Proceedings of the 2002 American Control Conference (IEEE Cat. No. CH37301), vol. 6. IEEE; 2002. p. 4555–9.

[60] Wan EA, Van Der Merwe R. The unscented Kalman filter for nonlinear estimation. In: Proceedings of the IEEE 2000 adaptive systems for signal processing, communications, and control symposium (Cat. No. 00EX373); IEEE; 2000. p. 153–8.

[61] Julier SJ, Uhlmann JK. New extension of the Kalman filter to nonlinear systems. Proceedings of the SPIE; 1997.

[62] Glorot X, Bengio Y. Understanding the difficulty of training deep feedforward neural networks. In: Teh YW, Titterington M, editors. Proceedings of the Thirteenth International Conference on Artificial Intelligence and Statistics, vol. 9. 2010. p. 249–56.

[63] Owen AB. Scrambling Sobol'and Niederreiter–Xing points. J Complex 1998;14(4):466–89.

[64] Rathore P, Lei W, Frangella Z, Lu L, Udell M. Challenges in training pinns: a loss landscape perspective, arXiv preprint arXiv:2402.01868, 2024.

[65] Mohtat P, Lee S, Sulzer V, Siegel JB, Stefanopoulou AG. Differential expansion and voltage model for li-ion batteries at practical charging rates. J Electrochem Soc 2020;167(11):110561. https://doi.org/10.1149/1945-7111/aba5d1.

[66] Prada E, Di Domenico D, Creff Y, Bernard J, Sauvant-Moynot V, Huet F. A simplified electrochemical and thermal aging model of lifepo4-graphite li-ion batteries: power and capacity fade simulations. J Electrochem Soc 2013;160(4):A616.

[67] Cai L, White RE. Lithium ion cell modeling using orthogonal collocation on finite elements. J Power Sources 2012;217:248–55.

[68] Forman JC, Bashash S, Stein JL, Fathy HK. Reduction of an electrochemistry-based li-ion battery model via quasi-linearization and pade approximation. J Electrochem Soc 2010;158(2):A93.

[69] Lai X, Zheng Y, Sun T. A comparative study of different equivalent circuit models for estimating state-of-charge of lithium-ion batteries. Electrochim Acta 2018;259:566–77.

[70] He H, Xiong R, Fan J. Evaluation of lithium-ion battery equivalent circuit models for state of charge estimation by an experimental approach. Energies 2011;4(4):582–98.

[71] Nejad S, Gladwin DT, Stone DA. A systematic review of lumped-parameter equivalent circuit models for real-time estimation of lithium-ion battery states. J Power Sources 2016;316:183–96.

[72] Jackey RA. A simple, effective lead-acid battery modeling process for electrical system component selection. In: SAE World Congress & Exhibition; SAE International; 2007. https://doi.org/10.4271/2007-01-0778

[73] Jackey RA, Plett GL, Klein MJ. Parameterization of a battery simulation model using numerical optimization methods. In: SAE World Congress & Exhibition; SAE International; 2009. https://doi.org/10.4271/2009-01-1381

[74] Jackey R, Saginaw M, Sanghvi P, Gazzarri J, Huria T, Ceraolo M. Battery model parameter estimation using a layered technique: an example using a lithium iron phosphate cell. In: SAE 2013 World Congress & Exhibition; SAE International; 2013. https://doi.org/10.4271/2013-01-1547

[75] Ahmed R, Gazzarri J, Onori S, Habibi S, Jackey R, Rzemien K, Tjong J, LeSage J. Model-based parameter identification of healthy and aged li-ion batteries for electric vehicle applications. SAE Int J Altern Powertrains 2015;4(2):233–47.
[76] Zheng L, Zhang L, Zhu J, Wang G, Jiang J. Co-estimation of state-of-charge, capacity and resistance for lithium-ion batteries based on a high-fidelity electrochemical model. Appl Energy 2016;180:424–34.
[77] González-Sopeña JM, Pakrashi V, Ghosh B. An overview of performance evaluation metrics for short-term statistical wind power forecasting. Renew Sustain Energy Rev 2021;138:110515.
[78] United States Environmental Protect Agency. Vehicle and fuel emissions testing: urban dynamometer drive schedules.
[79] Ai W, Kraft L, Sturm J, Jossen A, Wu B. Electrochemical thermal-Mechanical modelling of stress inhomogeneity in lithium-ion pouch cells. J Electrochem Soc 2020;167(1):013512.
[80] Subramanian S, Harrington P, Keutzer K, Bhimji W, Morozov D, Mahoney MW, Gholami A. Towards foundation models for scientific machine learning: characterizing scaling and transfer behavior. Adv Neural Inf Process Syst 2023;36:71242–62.